RSC Advances

PAPER

View Article Online
View Journal | View Issue

Cite this: *RSC Adv.*, 2025, **15**, 42272

Identification of interaction, surface species and anticorrosion potency for adsorption of myrrh extract on 330 stainless steel in 1 M HCl solution

Arafat Toghan, *[a] M. Fakeeh,[b] Ahmed Fawzy[c] and Hend S. Gadow *[b]

Steel and its alloys are essential materials in various industries, but they quickly react with the surrounding environment, especially humid ones, which leads to their destruction and corrosion on a large scale. Replacing synthetic organic inhibitors with plant-extracted or natural molecules has recently been a major challenge in terms of environmental and industrial aspects. In this report, the inhibitory dominance, adsorption of myrrh extract (MRE) as a green corrosion inhibitor on 330 stainless steel (SS) in 1.0 M HCl solution at the temperature range of 25 to 55 °C were explored. Weight loss (WL) measurements showed apparent inhibition efficiency (% IE) of MRE of up to 93.6% at 55 °C. The % IE values increased sharply with increasing inhibitor concentration and medium temperature. Adsorption investigations confirmed that the extract molecules were strongly adsorbed on the SS surface and were consistent with the Langmuir and Frumkin models. Polarization monitoring showed that the MRE behaves as a mixed-type inhibitor. EIS was also used to quantitatively evaluate the efficiency of the passive layer on the SS surface. All thermodynamic (ΔH, ΔS, ΔG) and kinetic (K_{ads}, E_a) parameters were calculated and analyzed. XPS was used to inspect the surface chemistry of SS and the nature of MRE-SS bonds. AFM demonstrated that the SS sample in the blank solution appears to be severely damaged and has the highest roughness of about 382.6 nm, compared to that obtained in the presence of MRE (145.61 nm). Various theoretical and computational methods were used to predict the performance of the examined inhibitor. All experimental findings of the different techniques are in excellent agreement with each other and with theoretical speculations. The outcomes of this study are thought to have some bearing on the sensible development of a potent inhibitor against the corrosion of metals in acidic environments.

Received 20th September 2025
Accepted 17th October 2025

DOI: 10.1039/d5ra07138k

rsc.li/rsc-advances

1 Introduction

Corrosion is a natural phenomenon that significantly affects the structural integrity of concrete and steel structures.[1–8] When infrastructures in sectors like petrochemicals and petroleum, which are vital to the world economy, are impacted, this becomes a problem.[9] The "cancer of metals" is a term used to describe metal corrosion,[10] which always leads to financial losses and security risks.[11] Implementing mitigation techniques has grown more crucial due to the significant impact of metal infrastructure loss due to corrosion during the past few decades. Cathodic protection,[11–13] anticorrosion coatings,[14] electroplating, and inhibitors[15–20] are a few methods of preventing corrosion. Because of their cheap operating costs and wide variety of applications, corrosion inhibitors have become the most practical and efficient way among the available approaches.[21–27] Nevertheless, conventional commercially used corrosion inhibitors including chromates, phosphates, and nitrates are hazardous to the environment and their surroundings.[28] Therefore, conventional corrosion inhibitors do not meet current environmental protection standards.[29] In order to overcome these obstacles, research into corrosion inhibitors has shifted in recent years towards the development of green corrosion inhibitors.[30–36] Researchers are searching for more ecologically benign compounds, also referred to as natural or green inhibitors, which include pharmaceuticals[31–36] and plant extracts,[37] are thought to be safe materials free of heavy metals.[38] Since the plant extracts are usually sourced sustainably and are less harmful to the environment and human health than conventional corrosion inhibitors, they are referred to as "green" extracts. These consist of amino acids, alkaloids, polyphenols, and frequently widely disseminated plant extracts with little economic value, such as agricultural waste and by-products of agro-industrial operations. Recent studies have shown that extracts of the *Cuminum cyminum* extract are effective in protecting metals/alloys in acidic

[a]*Chemistry Department, College of Science, Imam Mohammad Ibn Saud Islamic University (IMSIU), Riyadh 11623, Saudi Arabia. E-mail: aatahmed@imamu.edu.sa*
[b]*Higher Institute for Engineering and Technology, New Damietta 42519, Egypt. E-mail: hendgadow@gmail.com*
[c]*Chemistry Department, Faculty of Science, Assiut University, Assiut 71516, Egypt*

Table 1 Chemical ingredients of MRE[40,44]

Compounds	Structure	Formula	Percentage (%)
(**1**) Cyclohexene, 4-ethenyl-4-methyl-3-(1-methylethenyl)-1-(1-methylethyl)-, (3-*R*-*trans*)-	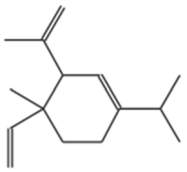	$C_{15}H_{24}$	0.3342
(**2**) Longifolene-(V4)	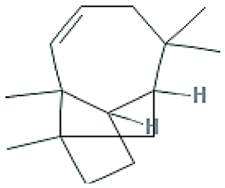	$C_{15}H_{24}$	4.0480
(**3**) Caryophyllene	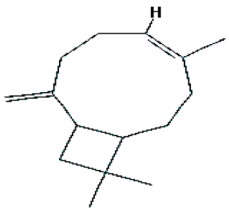	$C_{15}H_{24}$	0.2976
(**4**) 1,4-Methanoazulene, decahydro-4,8,8-trimethyl-9-methylene-, [1*S*-(1*à*,3*aá*, 4*à*,8*aá*)]$^{-}$	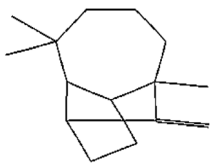	$C_{15}H_{24}$	1.047
(**5**) 1,6-Cyclodecadiene, 1-methyl-5-methylene-8-(1-methylethyl)-, [*s*-(*E*,*E*)]$^{-}$	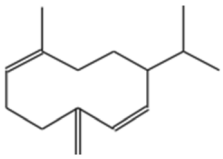	$C_{15}H_{24}$	0.3498
(**6**) Naphthalene, 1,2,3,5,6,7,8,8*a*-octahydro-1, 8*a*-dimethyl-7-(1-methylethenyl)-, [1*S*-(1*à*,7*à*,8*aà*)]$^{-}$	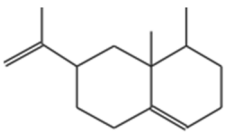	$C_{15}H_{24}$	0.3874
(**7**) Benzofuran, 6-ethenyl-4,5,6,7-tetrahydro-3,6-dimethyl-5-isopropenyl-, *trans*-	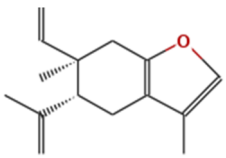	$C_{15}H_{20}O$	26.630
(**8**) 1*H*-Cycloprop[*e*]azulene, decahydro-1, 1,7-trimethyl-4-methylene-, [1*aR*-(1*aà*,4*aá*,7*à*,7*aá*,7*bà*]	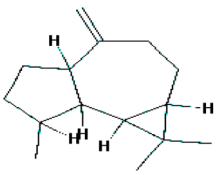	$C_{15}H_{24}$	0.5777
(**9**) Meso-hydrobenzoin	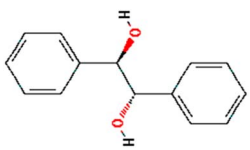	$C_{14}H_{14}O_2$	0.3437

Table 1 (*Contd.*)

Compounds	Structure	Formula	Percentage (%)
(**10**) 9(1*H*)-Phenanthrenone, 2,3,4,4*a*,10,10*a*-hexahydro-4*a*-methyl-, *cis*-	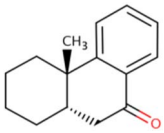	$C_{15}H_{18}O$	49.410
(**11**) Benzenemethanol, 3-methoxy-a-phenyl-	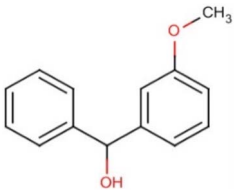	$C_{14}H_{14}O_2$	13.790
(**12**) Cyclohexanemethanol, 4-ethenyl-*à*,*à*, 4-trimethyl-3-(1-methylethenyl)-, [1*R*-(1*à*,3*à*,4*á*)]-	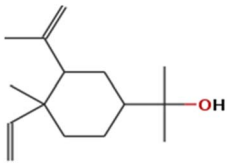	$C_{15}H_{26}O$	0.6306
(**13**) Testosterone	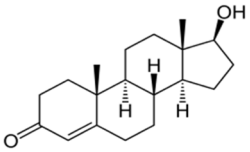	$C_{19}H_{28}O_2$	2.154

environments.[39] Noteworthy those flavonoids, alkaloids, polyphenols and others contain electron-rich atoms such as S, O, N and halogens as well as double bonds and aromatic rings, in their structures, which are frequently prevalent in plant extracts. These electron-rich sites allow them to be strongly adsorbed on the metal surface by donating lone pairs of electrons from heteroatoms and π-electrons of rings to the metal, preventing corrosive agents from reaching the metal surface and hindering the corrosion process, thus protecting it.

It's worth noting that myrrh trees are readily available in many countries, are inexpensive, and are abundant in production. In particular, MRE consists of various chemical compounds (listed in Table 1) that have been considered essential oils.[40,41] Interestingly, the percentage of this plant's extract reaches 15%. In fact, one kg of myrrh costs about 5–10 $, yielding 150 grams of extract, which is much less expensive (about one-tenth) than many other green inhibitors such as polysaccharide,[42] and *Ceratonia siliqua* L. seed oil.[43] Since 1 kg of myrrh raw material yields about 150 grams of extract which is enough to prepare 600 litters of 250 ppm MRE inhibitor. From an industrial perspective, its use as an anti-corrosion agent for metals/alloys is of economic and industrial value, given its effectiveness and low cost. The main challenge is its environmental compliance, as it is a low-toxic, biodegradable, and sustainable alternative. In contrast, traditional inhibitors often pose environmental and health risks due to their high toxicity. In this work a new green corrosion inhibitor extracted from myrrh plant was developed and applied to protect 330 SS in aqueous HCl for the first time at a temperature range of (25–55 °C). A number of theoretical and computational methods have been used to predict the effect and performance of this inhibitor as well.

2 Experimental

2.1 Materials

330 SS samples were used for all the corrosion measurements of this study. The chemical composition of 330 SS (% wt) is: Fe = 42, Ni = 36, Cr = 19, Mn = 2, Si = 1.13, $C = 0.080$, $P = 0.040$, and $S = 0.030$. Analytical reagent-grade HCl was diluted with deionized water to prepare 1.0 M HCl (blank) as a corrosive electrolyte stock. The process of creating a myrrh-based inhibitor (MRE) by extracting myrrh in methanol directly from its powder as explained in detail earlier.[44] In short, after the myrrh gum was completely dried, it was ground well into a fine powder. The powder was then dissolved in methanol and the solution was left for five days, filtering the solution, and then removing the methanol through distillation at 40 °C. The remaining concentrated material is then dried, making MRE ready for use in the corrosion experiments. Table 1 shows the main MRE components with their structures and proportions.[40,44] To prepare the stock solution of the inhibitor, 3.0 g of freshly prepared MRE was dissolved in 1 L of distilled water and

Table 2 Corrosion data obtained from WL measurements at different temperatures after 24 hours

Inh. conc. (ppm)	Δw (mg cm^{-2})	CR (mg cm^{-2} min^{-1})	θ	% IE	Δw (mg cm^{-2})	CR (mg cm^{-2} min^{-1})	θ	% IE
	25 °C				**35 °C**			
Blank	43.61	2.423	—	—	44.19	2.455	—	—
50	23.11	1.283	0.470	47.0	19.00	1.056	0.570	57.0
100	15.77	0.876	0.638	63.8	13.44	0.747	0.696	69.6
150	12.84	0.713	0.706	70.6	11.80	0.656	0.733	73.3
200	11.41	0.634	0.739	73.9	9.41	0.523	0.787	78.7
250	9.77	0.542	0.776	77.6	7.09	0.394	0.840	84.0
	45 °C				**55 °C**			
Blank	44.91	2.495	—	—	45.77	2.54	—	—
50	15.79	0.877	0.648	64.8	10.39	0.577	0.773	77.3
100	11.08	0.615	0.753	75.3	8.91	0.495	0.805	80.5
150	10.32	0.573	0.770	77.0	8.61	0.478	0.812	81.2
200	8.14	0.452	0.819	81.9	6.49	0.361	0.858	85.8
250	5.08	0.282	0.887	88.7	2.95	0.164	0.936	93.6

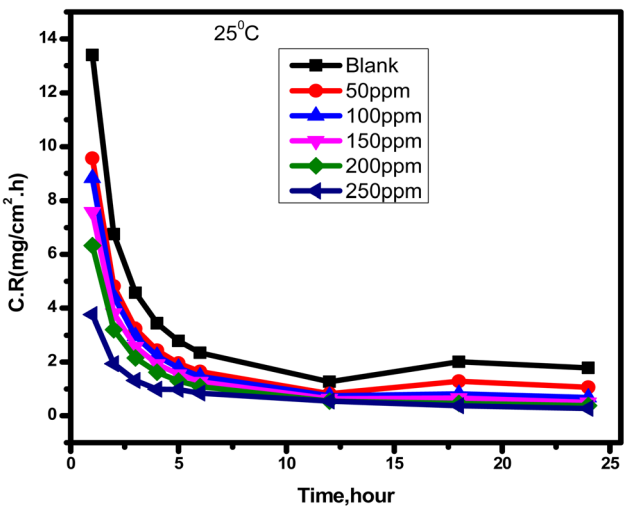

Fig. 1 Variation of CR of SS with time in 1.0 M HCl solution and in the presence of different concentrations of MRE at 25 °C.

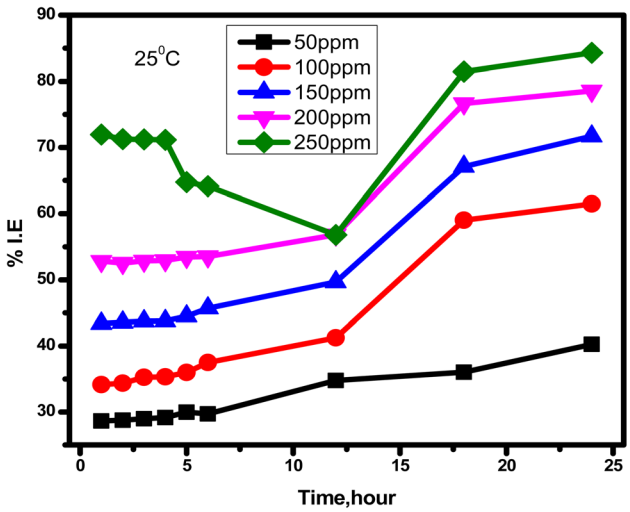

Fig. 2 Variation in % IEs of different concentrations of MRE in the corrosion of SS in 1.0 M HCl solution at 25 °C.

thus a concentration of 3000 ppm was ready. To perform inhibition tests, different concentrations of MRE (50–250 ppm) were prepared by dilution with distilled water.

Various experimental and computational techniques were used in this work. The experimental techniques are weight loss (WL), potentiodynamic polarization (PDP), open-circuit potential (OCP), electrochemical frequency modulation (EFM), linear sweep voltammetry (LSV) and electrochemical impedance spectroscopy (EIS). For surface analyses, atomic force microscopy (AFM) and X-ray photoelectron spectroscopy (XPS) were used. The computational prediction techniques are molecular dynamics (MD) simulations, density functional theory (DFT) calculations, molecular electrostatic potential (MESP), Mulliken atomic charges (MAC), and Fukui indices (FI).

2.2 Experimental techniques

2.2.1 Chemical measurements. Because the size homogeneity is essential for reducing experimental result variability, especially in surface-dependent investigations like corrosion inhibition. For WL tests, SS sheets with dimensions of 1 mm × 2 cm × 2 cm were used and therefore have the same exposure area (4 cm^2) to the corrosive environment. The SS specimens were successively polished using several grades of sandpaper in order to provide a smooth and uniform surface. After polishing, they were washed several times with distilled water and then acetone to remove any oils, grease, and organics that may be present on their surface. Finally, the cleaned SS samples were air-dried to remove any moisture that would accelerate deterioration. The samples were kept dry in a desiccator to protect

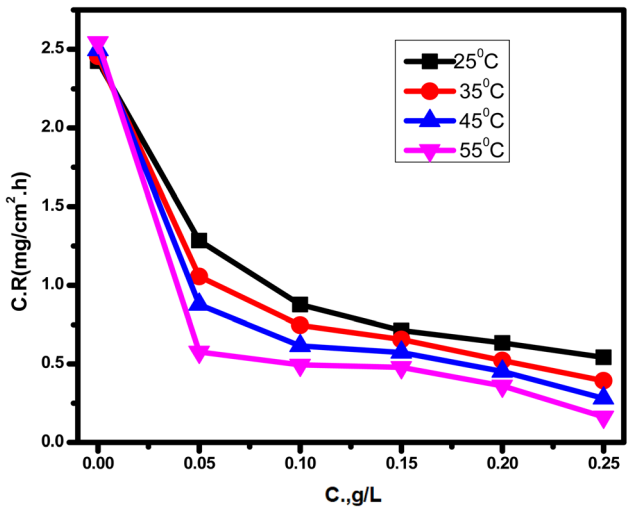

Fig. 3 Variation of CR of SS with MRE concentration in 1.0 M HCl solution at different temperatures.

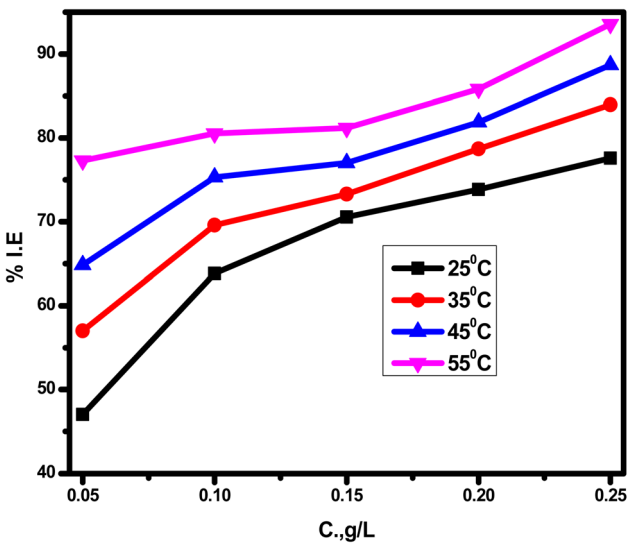

Fig. 4 Variation of % IE of MRE with its concentration in 1.0 M HCl solution at different temperatures.

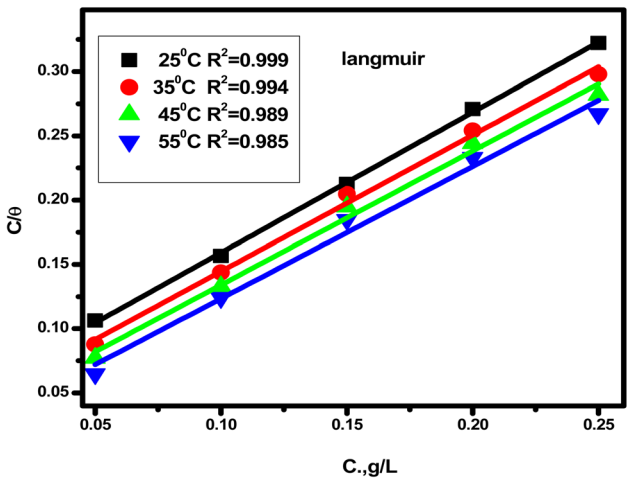

Fig. 5 Langmuir isotherm for adsorption of MRE molecules onto a SS surface in 1.0 M HCl solution at different temperatures.

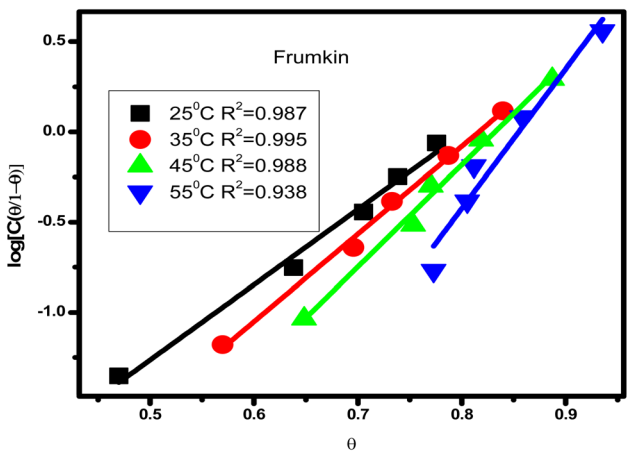

Fig. 6 Frumkin isotherm for adsorption of MRE molecules onto a SS surface in 1.0 M HCl solution at different temperatures.

them from moisture and any other potential contaminants to ensure they remained in the best possible condition and ready for accurate and reproducible investigations in corrosion experiments. The values of corrosion rates (CR) for SS in the absence and presence of MRE were calculated by:

$$\mathrm{CR} = \Delta w/A \times t \quad (1)$$

where, t is the immersion period (min), A is the specimen's exposed surface area (cm^2), and Δw is the mass loss (mg cm^{-2}). The IE (%), and the surface coverage (θ) were estimated by:[45]

$$\%\ \mathrm{IE} = [1 - (\mathrm{CR_{inh}}/\mathrm{CR_{uninh}})] \times 100 = \theta \times 100 \quad (2)$$

where, $\mathrm{CR_{uninh}}$ and $\mathrm{CR_{inh}}$ are the CR of SS in the uninhibited and inhibited media, respectively.

2.2.2 Electrochemical measurements (ECMs). For conducting all ECM, a Gamry instrument (PCI 300/4) potentiostat/galvanostat/ZRA was employed. This device has a Gamry framework system with ESA 400. For experimental running, the device is computer-controlled using three data collection software based on the behavioral ECM method: DC105 software for PDP, EFM140 software for EFM, and EIS300 software for EIS measurements. For plotting and fitting data, Echem Analyst 6.03 software was used. A traditional three-electrode cell was used: a saturated calomel electrode (SCE) as the reference electrode, a Pt gauze as the counter electrode and a square SS sheet (1.0 cm^2) as the working electrode (WE). The chamber was set up to maintain a consistent and measured temperature throughout each test. Before performing ECMs, the OCP is first

Table 3 Parameters obtained from Frumkin's and Langmuir's study

Langmuir					
Temp. (°C)	Log°K_{ads}	R^2	$-\Delta G_{ads}$ (kJ mol^{-1})	ΔH_{ads} (kJ mol^{-1})	ΔS_{ads} (J mol^{-1} K^{-1})
25	1.30	0.999	17.34	24.07	138.9
35	1.41	0.994	18.60		138.5
45	1.53	0.989	19.93		138.4
55	1.69	0.985	21.57		139.1

Frumkin						
Temp. (°C)	Log K_{ads}	R^2	α	$-\Delta G_{ads}$ (kJ mol^{-1})	ΔH_{ads} (kJ mol^{-1})	$-\Delta S_{ads}$ (J mol^{-1} K^{-1})
25	3.35	0.987	4.80	29.09	101.64	438.6
35	3.97	0.995	5.60	33.68		439.4
45	4.71	0.988	6.52	39.30		443.5
55	4.91	0.938	8.90	41.78		437.0

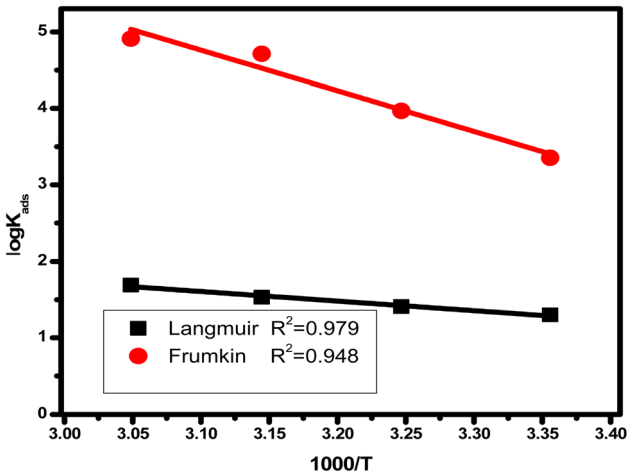

Fig. 7 van't Hoff plots for adsorption of MRE molecules onto SS surface in 1.0 M HCl solution.

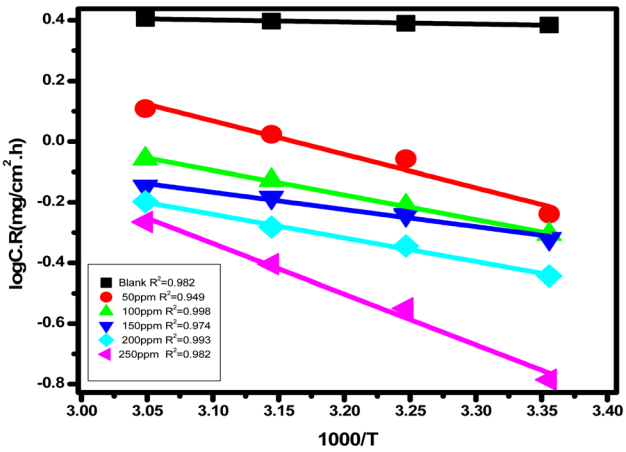

Fig. 8 Arrhenius plots for adsorption of MRE molecules onto SS surface in 1.0 M HCl solution at different MRE concentrations.

measured until it stabilizes over a period of 1800 s, as it serves as the starting point for the potential scan.

2.2.2.1 OCP. The change of OCP or E_{OC} *vs.* immersion time of SS in 1.0 M HCl solution without and with different concentrations of MRE at 25 °C over a period of 1800 seconds was examined.

2.2.2.2 PDP. In polarization tests, a voltage of −1.5 to 1.5 V is applied to the WE at a sweep rate of 0.1 mV^{-1} with a step increase of ±250 mV. All experiments were performed 3 times in freshly prepared solutions to check reproducibility. The % IE, and θ were calculated by:[46]

$$\% \text{ IE} = [(1 - i_{corr(inh)})/i_{corr(uninh)}] \times 100 = \theta \times 100 \quad (3)$$

Current density (i_{corr}) was determined by extrapolating the Tafel slopes (β_a, β_c) in the absence and presence of the inhibitor and was denoted by $i_{corr(uninh)}$ and $i_{corr(inh)}$, respectively. The Tafel slopes were determined by extrapolating the linear region of the anodic and cathodic curves in a potential range of ≈±50–100 mV relative to E_{corr}.

Table 4 Activation parameters obtained from Arrhenius's and transition state plots in the corrosion of SS in 1.0 M HCl solution in the presence of different MRE concentration

Inh. conc. ppm	E_a^* (kJ mol^{-1})	$-\Delta H^*$ (kJ mol^{-1})	$-\Delta S^*$ (J mol^{-1} K^{-1})	Log A
Blank	1.30	1.15	170.32	0.61
50	10.87	13.50	185.84	1.59
100	14.93	17.53	190.74	2.18
150	15.52	18.12	192.22	2.42
200	24.96	23.69	195.34	3.48
250	32.02	34.61	206.52	4.85

2.2.2.3 EIS. An identical cell configuration was used for EIS measurements *via* the ESA400 Gamry framework system. AC

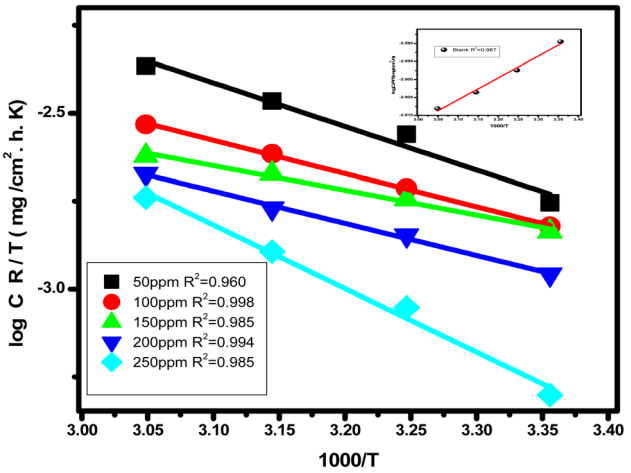

Fig. 9 Transition state plots for adsorption of MRE molecules onto SS surface in 1.0 M HCl solution at different MRE concentrations.

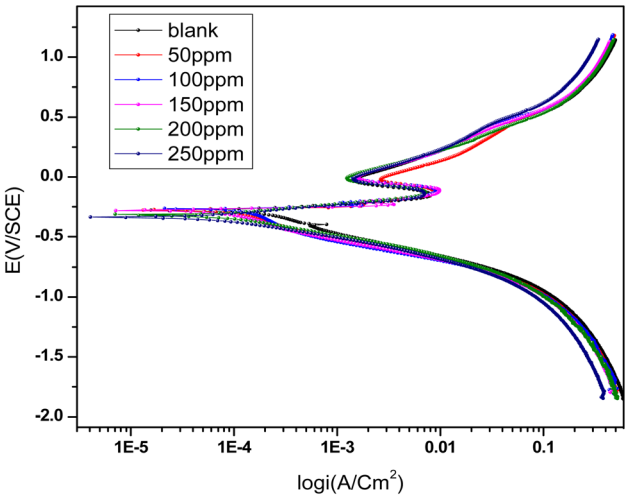

Fig. 11 PDP plots for SS in 1.0 M HCl solution and in the presence of different concentrations of MRE at 25 °C.

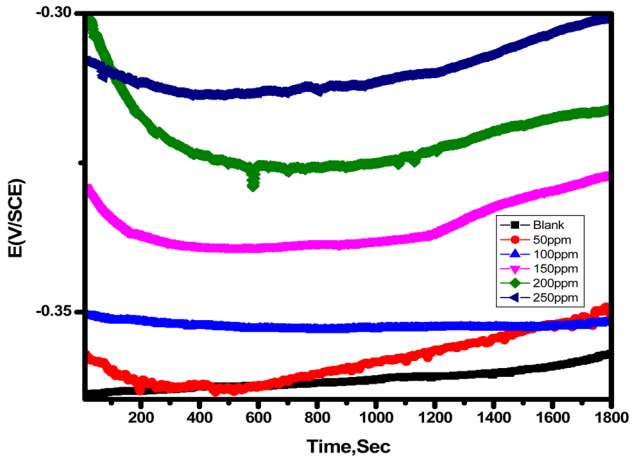

Fig. 10 OCP (potential *vs.* time) plots for SS in 1.0 M HCl solution and in the presence of different concentrations of MRE at 25 °C.

signals with a peak-to-peak amplitude of 5.0 mV were applied at the OCP over a frequency range of 100 kHz to 0.5 Hz. The Gamry Echem Analyst program was utilized to match all impedance data to the relevant equivalent circuit.

2.2.2.4 EFM. EFM tests were conducted using two sine waves at frequencies of 2.0 and 5.0 Hz and a potential disturbance signal of 10.0 mV amplitude. Three factors were taken into account when choosing the frequencies of 2.0 and 5.0 Hz.[46] Tafel slopes (cathodic = β_c and anodic = β_a), i_{corr}, and causation factors CF2 and CF3 were computed using the largest peaks.[47]

2.2.3 Surface analyses. SS samples were immersed in blank solution and in the presence of MRE inhibitor (250 ppm) for 1 day. Afterwards, the samples were taken out, rinsed thoroughly with deionized water, dried, and then ready for surface examination.

2.2.3.1 AFM. Using AFM analyses, it is possible to envisage the effect of corrosion and inhibition on SS surfaces. It was conducted with a Si_3N_4 probe (MLCT model; Bruker) in contact mode.

2.2.3.2 XPS. XPS is a powerful tool for screening and identifying the species present on the SS surface, which greatly helps in better understanding the inhibition mechanism and interactions. Thus, the nature of the chemical bond on its surface was systematically determined. It was performed with a K-alpha model instrument from Thermo Fisher Scientific, USA, using monochromatic Al K X-alpha radiation with an energy range of −10 to 1350 eV under pressures of 10^{-9} mbar, with a spot size of 400 μm, with full spectrum pass energy of 200 eV and a narrow spectrum pass energy of 50 eV.

2.3 Computational investigations

2.3.1 DFT calculations. Using DFT calculations derived from quantum chemical theories, possible inhibition mechanisms can be mathematically elucidated. It was implemented by the Dmol^3 module within Material Studio (version 7.0) to examine the full optimization of the geometry of the investigated MRE inhibitor. Undoubtedly, the electronic configurations and molecular structure of the extract reflect its effectiveness and behavior in the inhibition strategy. Using DFT computation, the quantitative parameters estimated are HOMO and LUMO molecular orbitals, dipole moment (μ), electronegativity (χ), absolute hardness (η), softness (σ), and electron affinity index (ω).[48]

2.3.2 MD simulation. MD simulations were used to theoretically investigate the possible interactions between MRE molecules and the SS surface. A Fe(110) surface with dimensions of (32.27 Å, 32.27 Å, 50.18 Å) consisting of 6 atomic layers within a 10 × 10 supercell featuring a 25 Å vacuum along the *C*-axis, within an HCl medium, was used. In comparison to other Fe surfaces, Fe(110) has the highest stabilisation and is a density packed surface. These experimental parameters were consistent with earlier studies.[49] The inhibitor molecules were

Table 5 Parameters obtained from PDP measurements (Fig. 11) at 25 °C

Inh. conc. (ppm)	$-E_{corr}$ (mV)	R_p (ohm)	i_{corr} (μA cm^{-2})	β_a (mV dec^{-1})	$-\beta_c$ (mV dec^{-1})	θ	% IE
Blank	279.0	9.3	2499.0	58.2	241.0	—	—
50	275.3	15.7	1414.0	49.0	233.3	0.121	12.1
100	266.0	17.5	1023.2	49.8	263.4	0.299	29.9
150	280.6	41.1	633.3	50.8	205.0	0.523	52.3
200	315.3	46.9	546.4	77.7	150.3	0.655	65.5
250	336.2	53.5	487.2	85.3	143.3	0.805	80.5

modeled and optimized through the Forcite software, after which the adsorption energy was calculated using the adsorption locator module. The simulation environment was maintained at a constant 25 °C using a Brandsen thermostat inside the NVT assembly, with a time step of 1.0 fs and a total simulation period of 300 ps under the COMPASS force field.[50]

2.3.3 MESP. MESP is an important computational method for accurately predicting and interpreting various aspects of interaction. Electrostatic potentials are depicted by color gradients at different locations on the electron density surface.

2.3.4 MAC and FI. The potential donor and acceptor sites of the active centers of MRE molecules can be further identified by applying MAC and FI methods.

3 Results and discussion

3.1 Experimental assessments

3.1.1 WL. WL experiments were implemented for SS samples in blank solution (HCl 1.0 M) and in the presence of different concentrations of MRE (50–250 ppm) at different temperatures (25–55 °C). The corresponding estimated corrosion parameters (Δw, CR, θ and % IE) are displayed in Table 2. Surprisingly, the %IE values increased sharply with increasing temperature (Fig. 4), indicating the possibility of chemical bond formation between MRE molecules and the SS surface. Fig. 1 shows plots of CR *versus* immersion time (1–24 h) at 25 °C. Meanwhile, the curves for temperatures from 35 to 55 °C are shown in the SI File (SF), see Fig. S2. It can be observed that the CR of SS decreased with prolongation of time and increase of concentration of inhibitory extract. While the %IE values increased significantly with increasing MRE concentration (Fig. 2). The variation in CR of SS at different temperatures is shown in Fig. 3. Fig. S1 in SF shows WL measurements *versus* immersion time.

3.1.2 Kinetics and thermodynamics. Based on the structure of MRE extract (Table 1), Their molecules are expected to be easily adsorbed on the SS surface and thus replace the H2O molecules adsorbed in the aqueous medium (blank), so the adsorption property here is carried out by the substitution process as follows:[51,52]

$$MRE_{(soln)} + xH_2O_{(ads)}/SS \rightarrow MRE_{(ads)}/SS + xH_2O_{(soln)} \quad (4)$$

In order to elucidate the mechanism of MRE inhibition, several isothermal models have been investigated, namely Frumkin, Temkin, Langmuir, Flory–Huggins, Freundlich, and

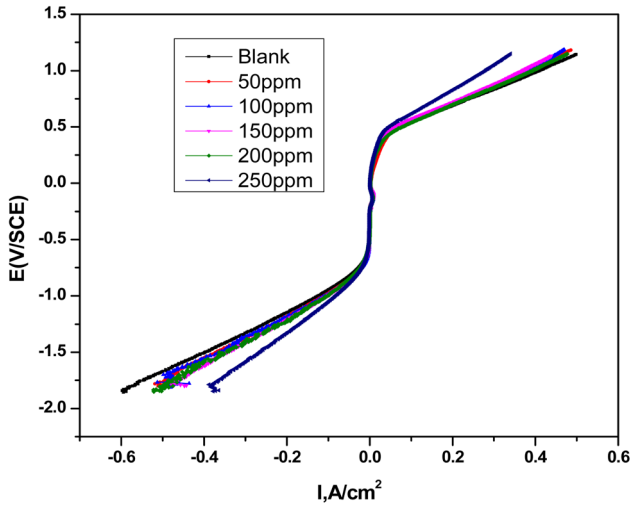

Fig. 12 LSV curves for SS in 1.0 M HCl solution and in the presence of different concentrations of MRE at 25 °C.

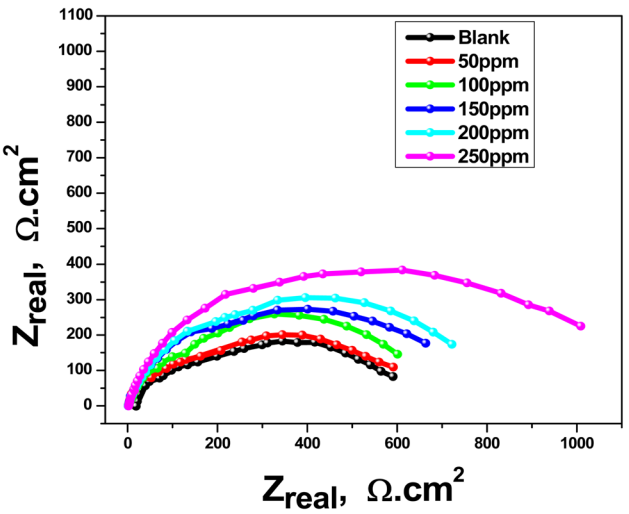

Fig. 13 Nyquist plots for SS in 1.0 M HCl solution and in the presence of different concentrations of MRE at 25 °C.

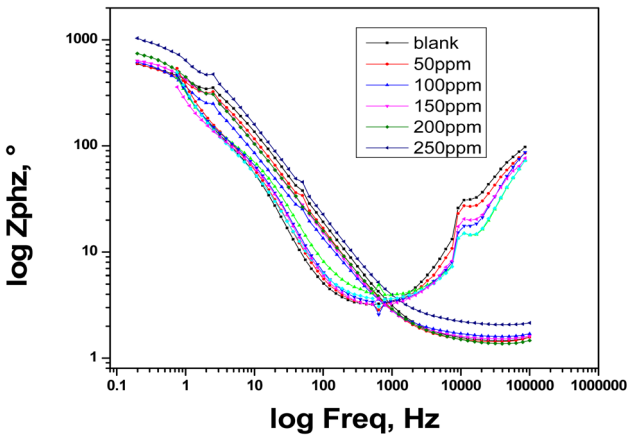

Fig. 14 BP plots for SS in blank solution (HCl 1.0 M) and in the absence and presence of different concentrations of MRE (50–250 ppm) at 25 °C.

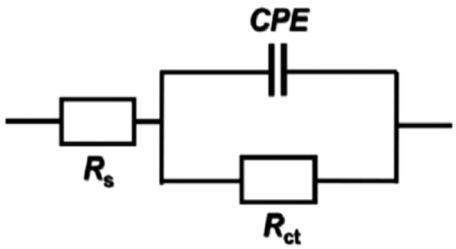

Fig. 15 Equivalent circuit proposed to fit the EIS experimental data.

Henry. Fig. 5 and 6 represent the best fit between the studied models, confirming that the MRE adsorption strategy can be understood through the Langmuir and Frumkin curves. Eqn (5) was used for the Langmuir model, and eqn (6) for the Frumkin model as follows:[53]

$$C_{inh}/\theta = (1/K_{ads}) + C_{inh} \quad (5)$$

$$\log(C_{inh}\,[\theta/(1-\theta)]) = \log K + 2\alpha\theta/2.303 \quad (6)$$

C_{inh} = MRE concentration, and equilibrium constant for adsorption = K_{ads}. Meanwhile, the Temkin, Flory–Huygens, Henry, and Freundlich isotherms are shown in the SF file (see Fig. S4).

Returning to Fig. 5, plotting C_{inh}/θ *versus* C_{inh} gives straight lines with slopes approaching one, intercepts equal to $(1/K_{ads})$, and correlation coefficient (R^2) values equal to one. The K_{ads} values were then calculated and summarized in Table 3, where the increase of their values with increasing temperature confirms the improvement of the adsorption and bonding strength of MRE molecules on the SS surface in agreement with the WL results.[53] For the Frumkin isotherm, plotting the $\log(C_{inh}\,[\theta/(1-\theta)])$ *versus* θ also gives straight lines with slopes approaching one (Fig. 6).

Then, the free energy of adsorption, ΔG_{ads}, was calculated using eqn (7):[54–56]

$$K_{ads} = 1/55.5e^{-\Delta G_{ads}/RT} \quad (7)$$

where, 55.5 = concentration of water (M = mol L^{-1}), R = gas constant (8.314 J mol^{-1} K^{-1}), and T (K). The plot of $\log K_{ads}$ *versus* $1000/T$ gives straight lines from which the values of ΔG_{ads} were determined and inserted in Table 3. Once the value of ΔG_{ads} is known, the kind of adsorption can be suggested. Both chemical and physical adsorption kinds are possible. For chemical adsorption, ΔG_{ads} should be > −40 kJ mol^{-1}, whereas for physical adsorption, it should be < −20 kJ mol^{-1}.[57,58] Examining the data in Table 3, we notice that the ΔG_{ads} values are temperature dependent and all are negative. These negative values confirm the spontaneity of the adsorption process. By Frumkin's study, at temperatures below 45 °C, the values were in the range −40 > ΔG_{ads} > −20 kJ mol^{-1} indicating a mixed (physical and chemical) nature of the adsorption. Interestingly, at temperatures above 45 °C, the ΔG_{ads} value was greater than −40 kJ mol^{-1}, confirming the formation of a chemical bond between the adsorbed MRE molecules and the SS surface, *i.e.*, it is purely chemisorption, which is in agreement with the WL and kinetic studies described before.

The enthalpy of adsorption (ΔH_{ads}) is computed by Van't Hoff equation,[59]

$$\log K_{ads} = -\Delta H_{ads}/(2.303 \times RT) + \text{constant} \quad (8)$$

when $\log K_{ads}$ is plotted against $1000/T$ (Fig. 7), it gives slopes equal to $-(\Delta H_{ads})/(2.303 \times R)$, and hence the ΔH_{ads} values were calculated (Table 3). It can be observed that the ΔH_{ads} values are positive indicating that the inhibition process is endothermic with chemisorption dominating.[60,61]

Table 6 Parameters obtained from EIS investigations at 25 °C

Inh. conc. (ppm)	R_{ct} (Ω cm^{-2})	R_S (Ω cm^{-2})	10^6 Y^0 (μΩ^{-1} S^n cm^{-2})	10^3 n	10^4 C_{dl} (F cm^{-2})	θ	% IE	χ^2
Blank	530.5	1.47	374.1	880	2.78	—	—	0.00032
50	599.5	1.43	295.2	875	2.44	0.115	11.5	0.00042
100	635.5	1.59	275.3	826	2.21	0.165	16.5	0.00015
150	650.6	1.52	221.6	862	1.96	0.185	18.5	0.00054
200	768.8	1.37	198.2	837	1.62	0.310	31.0	0.00037
250	982.1	1.43	174.2	812	1.31	0.459	45.9	0.00024

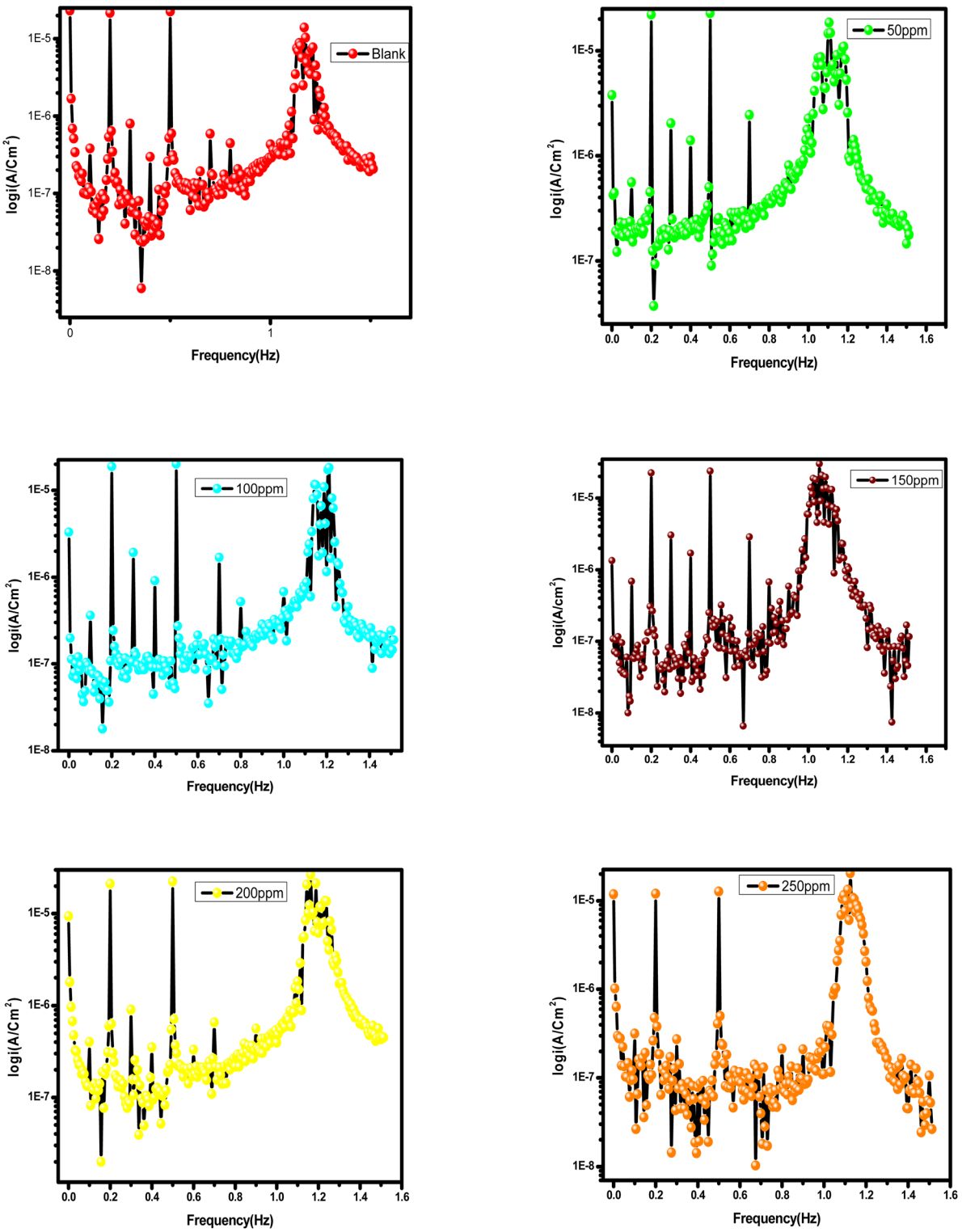

Fig. 16 EFM spectra for SS in 1 M HCl solution and in the presence of different concentrations of MRE at 25 °C.

The entropy of adsorption (ΔS_{ads}) is calculated by the following equation,[53]

$$\Delta G_{ads} = \Delta H_{ads} - T\Delta S_{ads} \quad (9)$$

Positive ΔS values (Table 3) indicate increased randomness of the system due to the preferred replacement of H_2O molecules (desorption) by MRE molecules (adsorption).[62] These findings confirm the strong and preferential adsorption of MRE

Table 7 Parameters obtained from EFM investigations (Fig. 16)

Inh. conc. (ppm)	i_{corr} (μA cm^{-2})	β_a (mV dec^{-1})	$-\beta_c$ (mV dec^{-1})	CF-2	CF-3	θ	% IE	CR mpy
Blank	39	79.09	130.10	2.19	3.086	—	—	17.82
50	21	48.98	54.11	1.911	3.27	0.461	46.1	9.60
100	18.73	46.67	65.55	2.222	3.57	0.519	51.9	8.56
150	17.46	58.61	88.2	2.27	2.95	0.552	55.2	7.98
200	13.27	38.03	41.5	2.23	3.08	0.659	65.9	6.60
250	9.207	47.64	49.47	1.955	3.13	0.763	76.3	4.21

molecules followed by the formation of a protective inhibitory layer on the SS surface, acting as anticorrosion barrier.

The Arrhenius equation was used to calculate the activation energy (E_a^*),[63]

$$\log \mathrm{CR} = \left(-E_a^*/2.303\ RT\right) + \log A \quad (10)$$

where, A is the Arrhenius constant. The Arrhenius plot shown in Fig. 8 gives straight lines, from their slopes the values of E_a^* were calculated and are listed in Table 4.

From the transition state equation,[64] the activation enthalpy (ΔH^*) and activation entropy (ΔS^*) are calculated as follows:

$$\ln\left(\frac{CR}{T}\right) = \left(\ln\frac{R}{Nh} + \frac{\Delta S^*}{R}\right) - \frac{\Delta H^*}{R}\frac{1}{T} \quad (11)$$

where, h = Planck's constant and N = Avogadro's number.

When $\log \mathrm{CR}/T$ was plotted against $1000/T$ (Fig. 9), straight lines were obtained. From the slopes and intercepts, the values of ΔH^* and ΔS^* were calculated, respectively (Table 4).[65]

Interestingly, adding 250 ppm of MRE (the inhibitor) to the blank solution (only 0.1 M HCl) resulted in a sharp increase in the E^* value from 1.30 to 32.02 kJ mol^{-1} (Table 4). Concurrently, the ΔH^* value changed from −1.15 to −34.61 kJ mol^{-1}. These results confirm that the addition of MRE forms a protective inhibitory layer on the SS surface, acting as a corrosion-resistant barrier.

3.1.3 Electrochemical measurements

3.1.3.1 OCP. Fig. 10 shows the variation in OCP of SS in blank solution (1.0 M HCl) and in the absence and presence of different concentrations of MRE (50–250 ppm) at 25 °C over a period of 1800 s. In the blank experiment, OCP values moved slightly toward positive values and quickly stabilized. Whereas when MRE was added, the OCP values first shifted towards the negative direction and then to the positive direction with stabilization, indicating that the anodic centres of the SS surface are the active adsorption sites of the extract molecules.

3.1.3.2 PDP. Tafel curves for SS in blank solution (HCl 1.0 M) and in the presence of different concentrations of MRE are depicted in Fig. 11. PDP test showed that the addition of MRE inhibitor effectively resisted SS surface corrosion by simultaneously suppressing the anodic (metal dissolution) and cathodic (*e.g.*, hydrogen evolution or oxygen reduction) reactions.[66,67] This may be due to the fact that inhibitor molecules are adsorbed onto the SS surface, blocking the oxidation/reduction sites that drive corrosion. As listed in Table 5, the sharp drop in the i_{corr} value from 2499.0 (blank) to 487.2 μA cm^2 (250 ppm MRE) is evidence for this action. As a result, a significant increase in %IE of up to 81% occurred, confirming the adsorption of MRE molecules onto the SS surface, thus blocking the active corrosion centers. Table 5 summarizes the calculated PDP parameters: %IE, anodic and cathodic Tafel slopes (β_a and β_c), corrosion current densities (i_{corr}) and corrosion potentials (E_{corr}). It has been reported[46,66] that an inhibitor is categorized as either anodic or cathodic type if the change in $\Delta E_{corr} > \pm 85$ mV and it is a mixed-type if $\Delta E_{corr} < \pm 85$ mV relative to E_{corr} value of the blank experiment. Its maximum value obtained here was 57 mV, confirming that MRE behaved as a mixed-type inhibitor. However, the preponderant anodic reaction control is indicated by the little change in E_{corr} values towards a positive route as MRE concentration increased. Additionally, there was no discernible change in the values of both β_c and β_a, suggesting that the two processes (anodic SS oxidation or corrosion and cathodic hydrogen reduction or evolution) were hindered without altering the mechanisms underlying the corrosion response.[65–67] The obtained anodic branches indicated limiting current densities at potentials positive of about 0 mV *vs.* SCE, evidence of the passivation nature of the 330 SS in the acidic medium. Hence, the effect of the inhibitor is measured mainly depending on the values of corrosion current densities (i_{corr}) near E_{corr}. The MRE is effective in inhibiting the corrosion process as the reduction in i_{corr} value with increasing the MRE concentration. Moreover, %IE values enhanced in tandem with the MRE concentrations. Increasing the MRE content improved the polarization resistance due to the preferred adsorption of MRE on the SS surface as shown in the LSV plots (Fig. 12).[68]

3.1.3.3 EIS. The interactions at the SS interface boundary under various circumstances, both before and after addition of myrrh extract, were examined using EIS. EIS improved understanding of the mechanisms underlying corrosion inhibition by offering vital insights into the electro-resistive and capacitive characteristics of the substrates.[69] The obtained EIS spectra were introduced as Nyquist (Fig. 13) and Bode (Fig. 14) plots. As shown in Fig. 13, the study analyses the Nyquist plots (NQs) for SS in aqueous HCl (1.0 M). In the examined corrosive

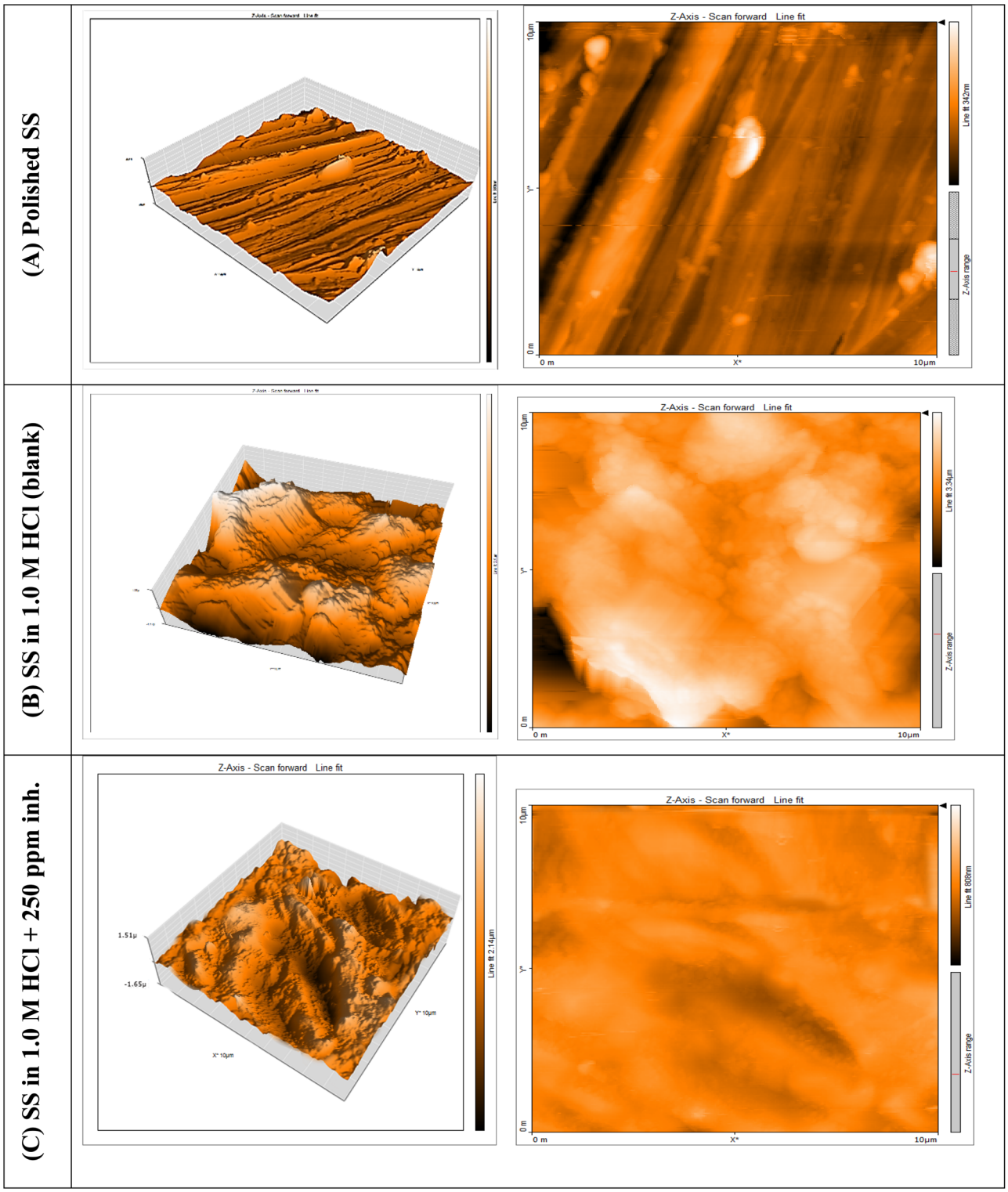

Fig. 17 AFM images of SS samples: (A) polished, (B) blank (immersed in 1.0 M HCl solution only), and (C) after adding 250 ppm of myrrh extract. Duration of corrosion/inhibition experiments = 24 h.

environment, MRE was discovered to improve the impedance response of SS; the NQs successfully demonstrated this behaviour. The semicircle size in the Nyquist plots significantly expanded in response to a rise in MRE concentration, suggesting the formation of a shielding barrier that lessens the SS contact with the corrosive environment.[70] Instead of the anticipated perfect circles, the Nyquist plots revealed the existence of non-ideal, twisted loops. Usually, this variation is

Table 8 Data obtained from AFM analysis (Fig. 17)

Surface	S_q (nm)	S_a (nm)	Max peak to valley height (nm)
Polished	40.02	28.22	373
1.0 M HCl (blank)	501.89	382.60	3560
1.0 M HCl + 250 ppm MRE	164.52	145.61	1097

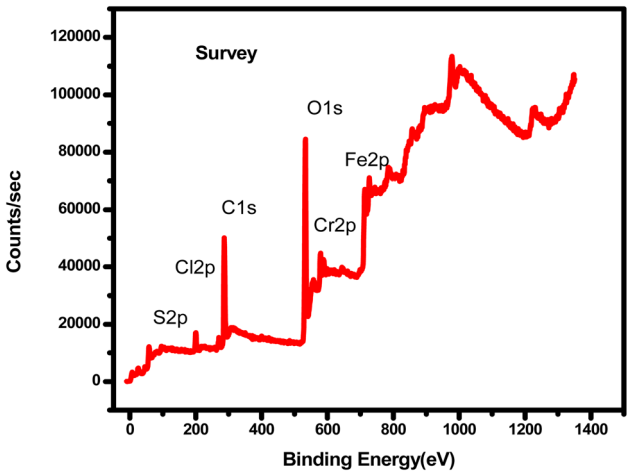

Fig. 18 XPS survey of the inhibited SS substrate in 1.0 M HCl with 250 ppm myrrh extract at 25 °C.

attributed to the SS surfaces' imperfections and heterogeneous properties.[71]

In this investigation, an appropriate equivalent circuit which was selected for the fitting of the acquired experimental findings in order to assess the electrochemical characteristics of the SS surface is shown in Fig. 15. Fitting the obtained experimental EIS data into the equivalent-circuit model produced the impedance values displayed in Table 6. A one-time constant in the Bode phase (BP) is depicted in Fig. 14. The figure demonstrates the fit of the line using the parametric circuit model and presents the impedance and phase data for SS exposed to HCl (1.0 M) at 25 °C as Bode plots. The majority of EIS spectra used in corrosion experiments have well-defined time constants for two capacitive semicircles or a low capacitive loop in the BP patterns. As can be shown, the corresponding CPE (constant phase element) models (see Fig. 14) are well fitted by the BP plots (Fig. 14) for myrrh extract. The Z_{CPE} value of the fitted circuit is calculated by:[72]

$$Z_{CPE} = 1/Y_0(j \times \omega)^n 11$$

R_p = polarization resistance, R_s = solution resistance, n = CPE exponent and Y_o = CPE constant. The value of n provides an insight into the inhibitor's nature. This value for the majority of organic inhibitors is between 0.8 and 1.0. On the other hand, with an ideal circuit, n will be 1.0. It was used in place of the circuit's best match to the experimental results. By replacing CPE with the values of double-layer capacitance (C_{dl}), such values for this circuit can be found:[73]

$$C_{dl} = [Y_0(R_p)^{1-n}]^{1/n} \quad (12)$$

A significant decrease in C_{dl} values brought on by the addition of the inhibitor suggests that metal–inhibitor adsorption has replaced metal–water adsorption. At the metal/corrosive medium interface, this leads to a decrease in the local dielectric constant and/or an increase in the thickness of the electric double layer. Additionally, the Bode plots (Fig. 14) showed only one phase maximum with a single-time constant; this could be the case when the charge transfer process takes place at the Fe–electrolyte interface. The significant adsorption of metal and inhibitor may be the reason for the progressive increase in the maximum phase angle at intermediate frequency when myrrh concentration rose. Additionally, the phase angle measurements showed surface roughness resulting from structural and interfacial origins, deviating somewhat from the ideal corrosive system (values of roughly 80).[74] By computing the values of % IE and θ, one may ascertain the degree of adsorption of MRE on the SS surface:[75]

$$\% \text{ IE} = [(R_{p(inh)} - R_{p(uninh)})/R_{p(inh)}] \times 100 \quad (13)$$

$$\theta = (R_{p(inh)} - R_{p(uninh)})/R_{p(inh)} \quad (14)$$

where, $R_{p(uninh)}$ and $R_{p(inh)}$ are the values of polarization resistance in the uninhibited and inhibited solutions, respectively. The values of R_p and % IE listed in Table 5 further demonstrated the adsorption of extract molecules on the SS surface. It was discovered that when the concentration of MRE increases, so did the measured values of R_p of the extract and, consequently, the values of %IE. The results demonstrate that, in 1.0 M HCl solution, the investigated MRE exhibited a good inhibitory action against the SS corrosion.

3.1.3.4 EFM. The EFM method can determine the current response using two sine waves of different frequencies for metal corrosion as shown in Fig. 16.[76] As reported earlier, the causality factors (CF-2 and CF-3) determine the validity of the EFM data and should be 0–2.0 and 0–3.0, respectively.[76] Table 7 illustrates the causation factors for the inhibitor are extremely near to the known values. Consistent with all the above measurements, with increasing MRE concentration, the CR rate of SS in this harsh environment decreased and an efficiency of up to 76% was achieved.

3.1.4 Surface analysis. Inspection the morphology, topography and species exist on a solid surface is an important and necessary step to fully understand the mechanism of action of an inhibitor in a corrosion experiment. Fig. 17 displays three AFM micrographs of SS specimens. Fig. 17a shows a polished, clean, and dried SS sample that appears uniform and smooth with a slight roughness of 28.217 nm (Table 8). To evaluate the surface after corrosion and inhibition experiments, the SS surface was checked after immersion for 24 h in HCl solution (1.0 M) in the absence (B) and presence of MRE inhibitor at a concentration of 250 ppm (C). The SS sample in the blank

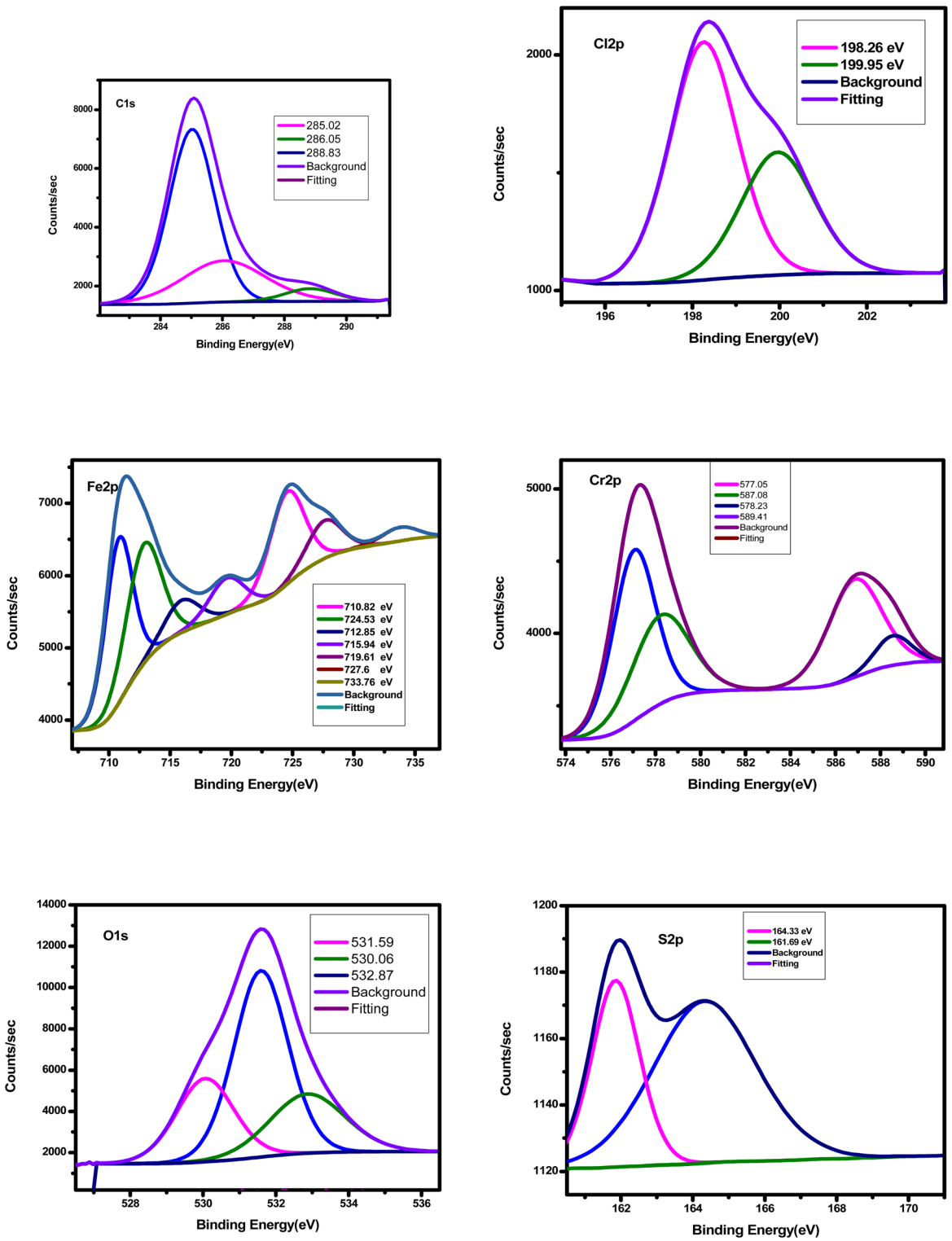

Fig. 19 High resolution XPS spectra of the inhibited SS surface (*i.e.* after immersion in 1.0 M HCl with 250 ppm of MRE at 25 °C).

experiments appears to be severely damaged and has the highest roughness of about 382.6 nm, compared to that obtained in the presence of MRE of 145.61 nm (Table 8). These results also demonstrated the effect of adsorption of MRE molecules on the SS surface, as they blocked most of the active corrosion sites.

The chemical composition of surfaces has not been investigated so far. Therefore, XPS was used to determine the

Table 9 Species present on the surface of the inhibited SS surface (*i.e.* after immersion in 1.0 M HCl with 250 ppm of MRE at 25 °C)

Species	BE (eV)	Components
C 1 s	285.02	C–Cl, C–C, C–H
	286.05	
	288.83	
Fe 2p	710.82	Fe_2O_3, $Fe2p_{1/2}$ of Fe^{3+}, FeOOH, Fe_2O_3,
	724.53	Fe 2p3/2 of Fe^{2+}, $FeCl_3$,
	712.85	ferric compounds satellites
	715.94	
	719.61	
	727.60	
	733.76	
Cl 2p	198.26	$FeCl_2$
	199.95	
O 1 s	531.59	Metal oxide, hydroxide, FeO and Fe_2O_3
	530.06	
	532.87	
S 2p	164.33	Sulfide
	161.69	
Cr 2p	577.05	Chromium oxide,
	587.08	chromium chloride, chromium hydroxide
	578.23	
	589.41	

surface composition and chemical bonding of MRE molecules on the surface. An XPS survey of SS in 1.0 M HCl with 250 ppm MRE at 25 °C would reveal the surface elemental composition and chemical states after the MRE has potentially formed a protective layer on the SS surface. As shown in Fig. 18, the XPS scan shows peaks corresponding to the elements present in the SS substrate (*e.g.*, Fe, Cr, and S), and any elements of MRE with an emphasis on essential species such as C and O. The binding energies of these elements would help determine how the MRE molecules have adsorbed and chemically bonded to the steel surface, indicating the nature of the protective layer that mitigates corrosion. Fig. 19 displays the high resolution XPS spectra of the inhibited sample showed characteristic peaks that were recognized as C 1s, Cl 2p, Fe 2p, O 1s, Cr 2p and S 2p. The complying assignments and binding energies (BE, eV) for each peak constituent are provided in Table 9. Spectra of C 1 s may be attributed to C–H–, C–C–, and C–Cl bonds at 285.02, 286.05, and 288.83 eV for samples that were maintained with MRE inhibitor.[77,78] The appearance of a chlorine peak on the SS surface treated with MRE in 1.0 M HCl solution is caused by the interaction of chloride ions with the positively charged SS surface.[79] The Cl 2p spectra of the inhibited SS samples showed two peaks for Cl $2p_{3/2}$ at 198.26 and additional peaks for Cl $2p_{1/2}$ at 199.95 eV, indicating the presence of a Fe–Cl bond in $FeCl_3$.[80] Seven peaks were seen in the Fe 2p XPS spectra of the inhibited SS samples. The origins of these peaks were determined to be Fe $2p_{3/2}$ of Fe^{2+} at 710.82 eV, Fe $2p_{3/2}$ of Fe^{3+} at 712.85 eV, Fe $2p_{3/2}$ satellites of Fe^{2+} at 719.61 eV, and Fe $2p_{1/2}$ of Fe^{2+} at 727.6, 733.76 eV. Furthermore, the high-resolution O 1s spectra of the SS samples treated with the MRE inhibitor display three distinct peaks. The first peak, designated as O^{2-} at 530.06 eV, is associated with the oxygen atoms that are coupled to Fe^{2+} and Fe^{3+} in the FeO and Fe_2O_3 oxides.[81] At 531.59 and 532.87 eV, the second and third peaks are attributed to OH^- and might be connected to Fe^{3+} in FeOOH.[82,83] In fact, chromium was found in myrrh extract at a very low concentration of 0.001148% (11.48 ppm) by ICP-MS analysis of the inorganic constituents of MRE.[84] The chromium signal appearing in the XPS spectrum of a myrrh-coated SS substrate likely originates from the SS itself, which is a Cr-rich alloy (Cr = 19%), and its presence is confirmed by the signal at specific binding energies in the spectrum. Thus, Cr 2p is linked to peaks with energies of 577.05, 587.08, 578.23, and 589.41 eV in Cr-oxide, Cr-chloride, and Cr-hydroxide. However, the sulfur signal in the XPS spectrum of the MRE-coated SS substrate may come either from the MRE or from the SS itself. Returning to the data shown in Table 1,[40] and the ICP-MS/GC-MS analyses of the inorganic–organic ingredients of MRE,[84] the possibility that the S-signal came from the MRE extract is excluded as it is not present in its constituents. Interestingly, recent FT-IR (Fourier transform infrared) analyses of the Al surface inhibited by methanolic myrrh extract in 1 M HCl showed no evidence of *S*-containing groups.[85] Therefore, the S-signal is likely to originate from the SS substrate. The MRE inhibitor's adsorption on the SS surface in 1.0 M HCl solution is supported by these XPS study results.

3.2 Computational investigations

DFT is a very useful calculation for predicting the inhibition strength of different molecules such as MRE.[86,87] Then, the electrical properties of MRE were calculated and presented in Tables 10 and S1, S2 of the SI File. Given the fact that E_{HOMO} is associated with electron donating capacity, increasing its values would enhance the effectiveness of the inhibitor.[88,89] It is very interesting that MRE molecules occupy the highest value of HOMO, which would be the reason for the large inhibitory activity (Table 10). Meanwhile, the low E_{LUMO} value indicates that the inhibitor molecules can locate another negative charge on the SS surface, as the capacity to accept electrons is essential to E_{LUMO}. The inhibitors under study have comparatively high LUMO values and high E_{HOMO} values. The 13 MRE molecules studied were found to be highly effective because they interacted while acting as donors. The metal functions as a donor to the inhibitor molecules, lowering the inhibitor effectiveness while increasing the metal reactivity, even if the inhibitor molecules with a modest E_{HOMO} value decrease metal reactivity. $E_{HOMO} - E_{LUMO}$ showed that the evaluated inhibitor chemicals had the best corrosion inhibition (Fig. 20, S5 and S6). Significant inhibitory action was shown by the high softness and low hardness values of the inhibitor compounds with a high E_{HOMO} and a low energy gap. The χ values of MRE molecules may provide insight into the nature of the bond between them and the SS surface.[90] Iron atoms will create chemical connections by acquiring electrons from inhibitor molecules, according to the research on the inhibitory effects of inhibitor molecules intended as iron-inhibitors (Tables 10, S1 and S2). According to the χ

Table 10 Parameters computed by DFT for neutral MRE molecules

	Compound				
Parameter	(1)	(2)	(3)	(4)	(5)
$-E_{HOMO}$ (eV)	−5.005	−5.031	−5.153	−5.087	−5.018
$-E_{LUMO}$ (eV)	−0.179	0.145	−0.367	0.114	−0.214
ΔE (eV)	4.826	4.890	4.790	4.973	4.800
η (eV)	2.410	2.450	2.395	2.49	2.400
σ $(eV)^{-1}$	0.414	0.408	0.418	0.402	0.416
Pi (eV)	−2.590	−4.890	−5.520	−4.973	−5.230
χ (eV)	2.590	4.890	5.520	4.973	5.230
Dipole moment, μ	1.157	0.4177	1.043	0.7814	1.2400
Molecular area ($Å^2$)	261.279	232.595	241.841	229.501	262.693
ω (Electrophilicity index)	1.390	4.960	6.360	4.970	5.700
ω^+ (Electro-accepting power)	0.397	0.382	0.510	0.370	0.417
ω^- (Electro-donating)	2.990	2.970	3.270	2.870	3.030
ε (Nucleophilicity index)	0.716	0.201′	0.157	0.032	0.175
ΔE back donation	−0.603	−0.613	−0.599	−0.623	−0.600
ΔN_{max} (e)	0.350	−0.136	−0.256	−0.139	−0.197

	Compound				
Parameter	(6)	(7)	(8)	(9)	(10)
$-E_{HOMO}$ (eV)	−5.046	−4.695	−5.175	−5.896	−5.295
$-E_{LUMO}$ (eV)	0.146	−0.205	0.146	−1.302	−2.042
ΔE (eV)	4.900	4.490	5.030	4.590	2.550
η (eV)	2.450	2.250	2.520	2.300	1.280
σ $(eV)^{-1}$	0.410	0.400	0.397	0.435	0.781
Pi (eV)	−4.900	−4.900	−5.030	−7.198	−7.340
X (eV)	4.900	4.900	5.030	7.198	7.340
Dipole moment, μ	0.7915	1.6092	2.150	3.6220	5.555
Molecular area ($Å^2$)	249.88	254.63	250.150	232.910	234.920
ω (Electrophilicity index)	4.900	5.340	5.020	11.260	21.045
ω^+ (Electro-accepting power)	0.383	0.074	0.391	0.133	0.210
ω^- (Electro-donating)	3.483	2.761	3.050	4.906	6.170
ε (Nucleophilicity index)	0.204	0.187	0.199	0.089	0.048
ΔE back donation	−0.613	−0.563	−0.630	−0.575	0.320
ΔN_{max} (e)	−0.126	−0.137	−0.148	−0.634	−1.195

	Compound		
Parameter	(11)	(12)	(13)
$-E_{HOMO}$ (eV)	−5.047	−5.227	−5.135
$-E_{LUMO}$ (eV)	−0.935	0.020	−1.903
ΔE (eV)	4.110	5.027	3.230
η (eV)	2.060	2.510	1.620
σ $(eV)^{-1}$	0.485	0.398	0.617
Pi (eV)	−5.982	−5.207	−7.038
X (eV)	5.982	5.207	7.038
Dipole moment, μ	4.0833	2.7910	8.3783
Molecular area ($Å^2$)	249.595	260.61	290.039
ω (Electrophilicity index)	8.690	5.400	15.290
ω^+ (Electro-accepting power)	0.937	0.335	2.273
ω^- (Electro-donating)	3.928	3.016	5.792
ε (Nucleophilicity index)	0.110	0.185	0.065
ΔE back donation	−0.515	−0.628	−0.405
ΔN_{max} (e)	−0.413	−0.185	−0.851

value, the inhibitor works well even when it has a low value. The investigated inhibitor molecules work better, as indicated by the ΔN value in Tables 10, S1 and S2, which demonstrates that they transfer more electrons to the Fe atoms on the metal surface. Another distinct parameter displays in Tables 10, S1 and S2 is dipole moment (μ). The IE indicates that a large μ

indicates substantial corrosion inhibition potency, even if prior research has not established a significant association between μ and IE. Lowering the μ value was proven to boost corrosion IE in many experiments. Since the evaluated inhibitor's μ value is low, it indicates that the metal surface is coated more firmly. Because they expand the area in which they may interact with the SS surface, larger MRE molecules have a stronger inhibitory impact. In terms of the nucleophilicity index (ε), we found that the neutral form of the MRE components had greater numerical values than the protonated form. As a result, MRE components in their neutral state exhibit strong nucleophile, indicating that the neutral form can help electrons adhere to the SS surface. Recently, the electrical donor capacity ($\omega^- = (3I + A)^2/16\ (I - A)$) and the electrical receiver capacity ($\omega^+ = (I + 3A)^2/16\ (I - A)$) have been used to assess PPE's capacity to transmit or receive electrical charge.[91] The positive attributes of hardness (η) and, consequently, the negative attributes of (E_{BD}) (back donation energy $= -\eta/4$) are pivotal indicators of and charge transfer/electron donation dynamics from iron PPE molecules.

The adsorption locator module has been identified as the most suitable structure (adsorbent) within the corrosion-simulating fluid (comprising 250 H_2O molecules, along with 10 H_3O^+ and 10 Cl^- ions) for the adsorption of MRE (adsorbate) onto the Fe(110) crystal. The methodologies for the adsorption of MRE molecules, in both neutral, protonated and vacuum forms, are depicted in Fig. 20, S7 and S8, respectively, illustrating the top and lateral perspectives of the Fe(110) substrate. Tables 11, S3 and S4 enumerate the results obtained from the MD simulation concerning deformation, solid adsorption, and the overall energetic states. The calculations aim to ascertain the E_{total} pertinent to the substrate and MRE by aggregating molecular energies derived from solid adsorption alongside distortion energies. The energy quantified during the detachment of a single adsorbate particle from the adsorbent substrate is represented by dE_{ads}/dN_i. Their values associated with the MRE components exceed those related to water molecules, suggesting that MRE exhibits a stronger adsorption affinity than water. Consequently, it is anticipated that the MRE components will adhere to the SS surface, thereby forming a passive layer that safeguards the metallic substrate against acidic corrosion. According to Tables 11, S3 and S4, along with prior empirical investigations,[92,93] the components of the MRE demonstrate elevated adsorption energies and exhibit commendable performance within the solution matrix. A meticulous examination indicates that the molecular configuration of the local molecule is oriented parallel to the SS surface.[94] To enhance the contact area or surface coverage efficacy of SS, the components of the MRE are expected to adopt this specific adsorption behaviour. Rather than facilitating undesirable attacks by Cl^{-1}, the expanded SS/myrrh contact zone will restrict substrate accessibility.[95,96] It is hypothesized that electron transfer from the SS surface to the MRE components transpires in a retrograde manner, thereby reversing the reaction, particularly in the presence of a charged protonic component. Theoretical analyses substantiate that MRE components exhibit a strong adsorption affinity for the SS surface, resulting in the formation of durable adsorbent

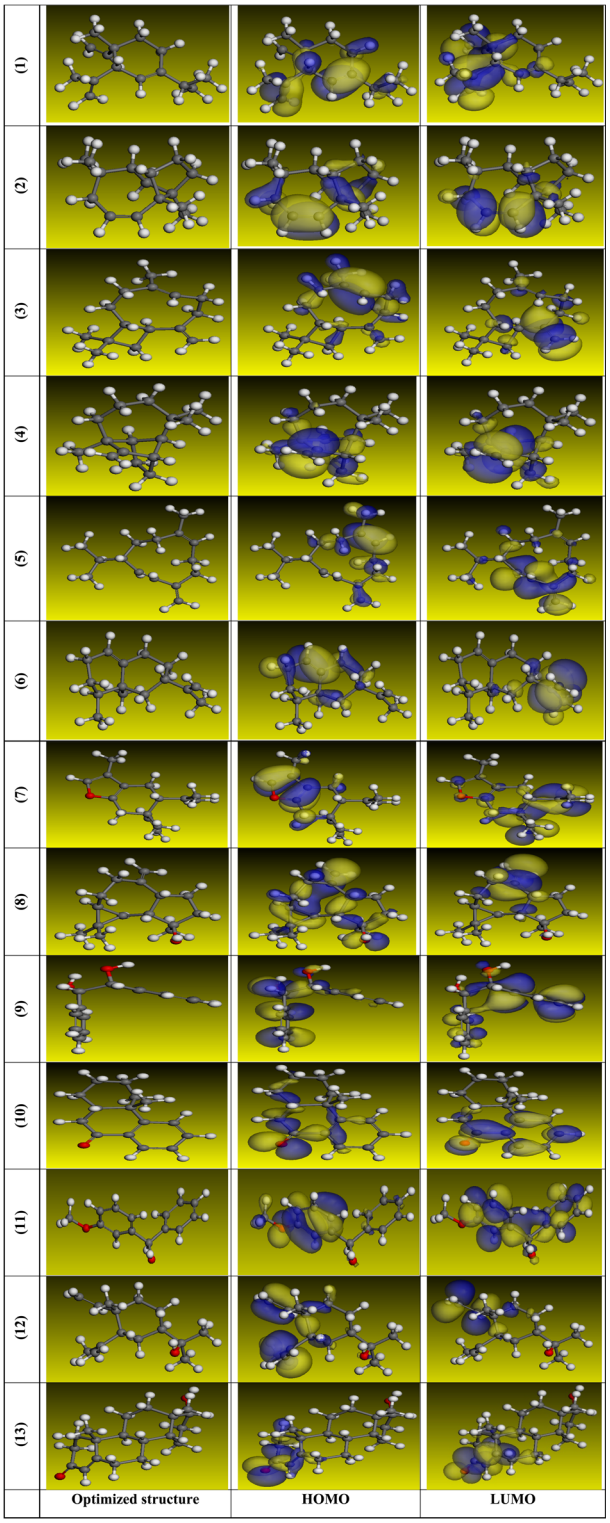

Fig. 20 Optimized structures, LUMO and HOMO for the 13 neutral MRE molecules.

coatings that protect the SS substrate from corrosion induced by HCl solutions. Fig. 21, S7 and S8, in conjunction with Tables 11, S3 and S4, illustrate the adsorption dynamics of MRE molecules in both vacuum and acidic (neutral and protonated)

Table 11 Parameters computed by MD simulation for MRE molecules

	Compound				
Parameter (kcal mol^{-1})	(**1**)	(**2**)	(**3**)	(**4**)	(**5**)
Total energy	−5156.390	−5.112	−4257.168	−6938.518	−6874.990
Adsorption energy	−5130.234	−5092.202	−4244.306	−6917.882	−6875.450
Rigid adsorption energy	−5317.082	−5271.337	−4.426	−7110.053	−7057.550
Deformation energy	186.850	179.130	181.600	192.170	182.100
dE_{ads}/dN_i	−110.960	−55.440	−105.160	−94.230	−111.740
dE_{ads}/dN_i for water	−9.490	−7.710	−10.530	−8.200	−9.720

	Compound				
Parameter (kcal mol^{-1})	(**6**)	(**7**)	(**8**)	(**9**)	(**10**)
Total energy	−6866.785	−6890.549	−6852.649	−6749.567	−6900.022
Adsorption energy	−6842.330	−6874.151	−6901.110	−6775.957	−6893.540
Rigid adsorption energy	−7031.989	−7069.073	−7097.571	−6964.140	−7090.820
Deformation energy	189.660	194.920	196.460	188.180	197.280
dE_{ad}/dN_i	−1.670	−116.970	−93.800	−114.170	−122.220
dE_{ads}/dN_i for water	−9.820	−7.700	−13.770	−9.340	−10.500

	Compound		
Paramete (kcal mol^{-1})	(**11**)	(**12**)	(**13**)
Total energy	−6907.988	−6954.281	−6971.699
Adsorption energy	−6.928.218	−6902.147	−6902.404
Rigid adsorption energy	−7135.060	−7098.410	−7095.140
Deformation energy	206.840	196.260	192.730
dE_{ad}/dN_i	−129.220	−103.620	−121.600
dE_{ads}/dN_i for water	−8.620	−10.840	−11.890

environments. The adsorption energies in the context of an aqueous solution surpass those in a vacuum environment, indicating a more effective adsorption of myrrh molecules onto the SS surface. To quantify the energy associated with the adsorption of MRE onto the SS(110) interface, the following equations may be employed:[97,98]

$$E_{binding} = -E_{interact} \quad (15)$$

$$E_{interact} = E_{tot} - (E_{sub} + E_{inh}) \quad (16)$$

E_{sub} = energy contributions from both water molecules and the substrate.

Predominantly, regions exhibiting negative electrostatic potential are represented in red, indicating areas of significant electrical activity and electrophilicity. The majority of heteroatoms (O, N) and conjugated double bonds can be observed in regions of high electron density. Functional groups containing oxygen serve as indicators of zones that facilitate electrophilic attacks through negative potential. Fig. 22, S9 and S10 illustrate the nucleophilic attack on the H atoms (blue) of the 13 molecules of MRE according to MESP investigations.

It is worth noting that the active sites in MRE structures are regions that show an increased propensity to interact with the SS substrate. Fig. 23 delineates a comparable behavioral trend, wherein the total negative charge (TNC) escalates concomitantly with the protonation of the MRE molecules.[90] An augmentation in the structural interaction among protonated entities is observable through the electrostatic attraction that exists between the protonated components and the Cl^{-1} that have been adsorbed onto the SS surface.[53] Organic components of myrrh extract, inclusive of heteroatoms, have the ability to undergo protonation in aqueous HCl, thus producing positively charged entities. They can then engage in interactions with the Cl^{-1}, which diffuses abundantly across the metal surface. Fig. 24 and S11 delineate the atomic structures of the MRE components under examination, highlighting elevated values of Fukui functions (f_k^+ and f_k^-) in both protonated and non-protonated scenarios, serving as supplementary indicators (FI). The findings indicate that each molecular entity possesses distinctive atoms pertinent to both electrophilic and nucleophilic frameworks. The LUMO, representing the molecular segment with the most significant f_k^+, exhibits augmented reactivity towards donor reagents and is consequently predisposed to nucleophilic assault. The atom within the target molecule that exhibits the highest f_k^- values, correlated with HOMO, facilitates reactivity directed towards an acceptor species, culminating in electrophilic engagement. The presence of protons (H^+) obstructing the atomic centres in the protonated configuration results in a diminution of f^- values for the

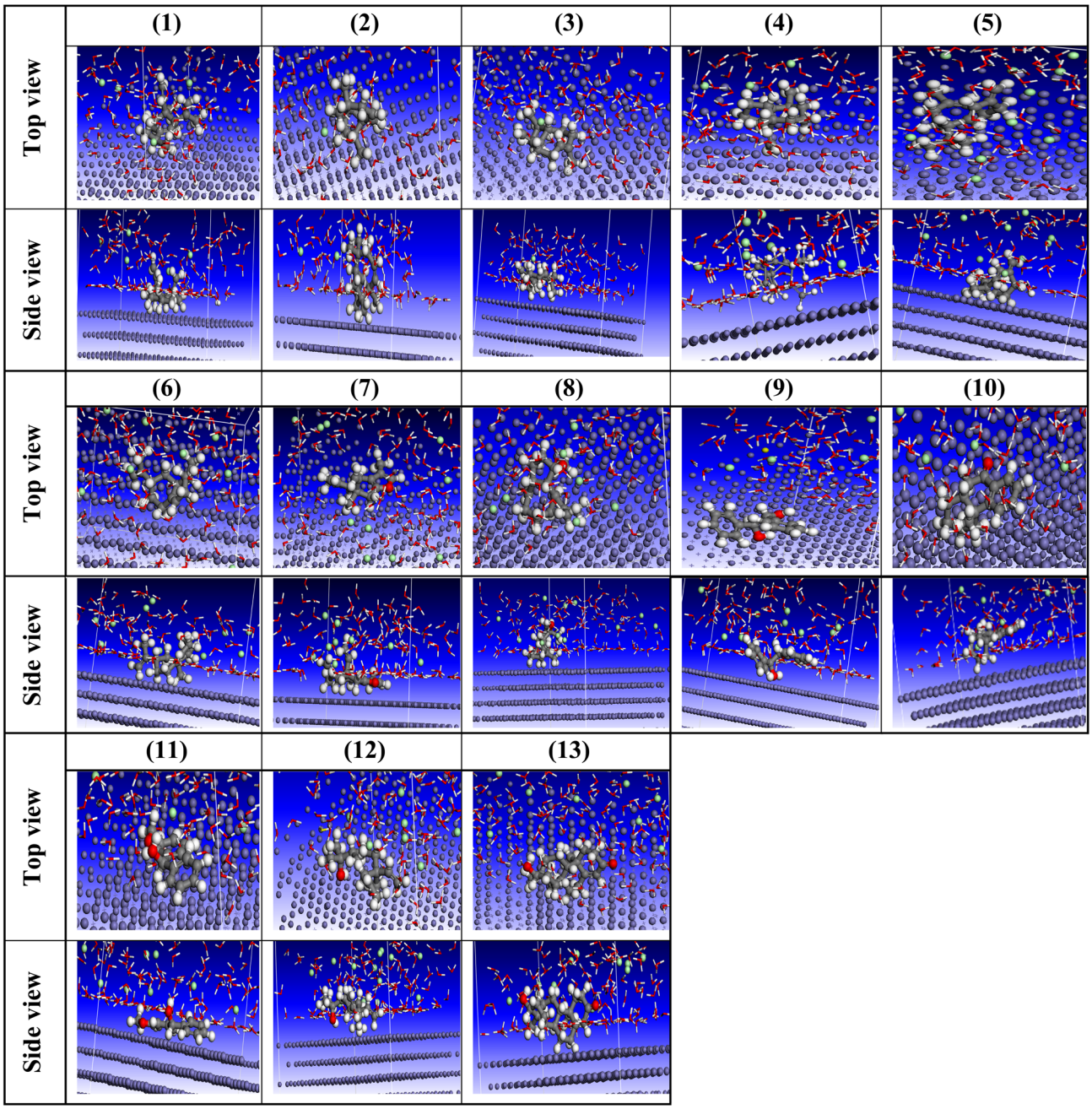

Fig. 21 Top and side views of the most stable adsorption configuration of the 13 molecules of MRE computed using MD simulation on Fe(110) substrate.

corresponding atoms, whereas the f^+ values for the entities experience an upsurge owing to the atoms' enhanced capacity for electron acceptance (Fig. 24 and S11). Moreover, altered atoms within analogous components manifest divergent f^+ and f^- values, thereby signifying that the MRE exhibits a dual effect.

3.3 The inhibition mechanism

The efficiency of a corrosion inhibitor is determined by its adsorption capacity and its bond strength to the surface of the material. Myrrh extract contains 13 compounds (Table 2) with unique structures that undoubtedly make it a promising green corrosion inhibitor. Statistical calculations (MD and DFT) verified that the inhibitory properties of the MRE originate from the electron-dense active sites, such as the π-bond of the benzene ring, OH group, and C=O. These sites enable MRE species to form bonds with the SS surface and protect it. Functional groups in organic molecules are most likely to accept a proton in aqueous acidic solutions and be protonated.[98] Based on the MRE structure, the SS surface is expected to be significantly protected either by: (i) Electrostatic interactions occur between

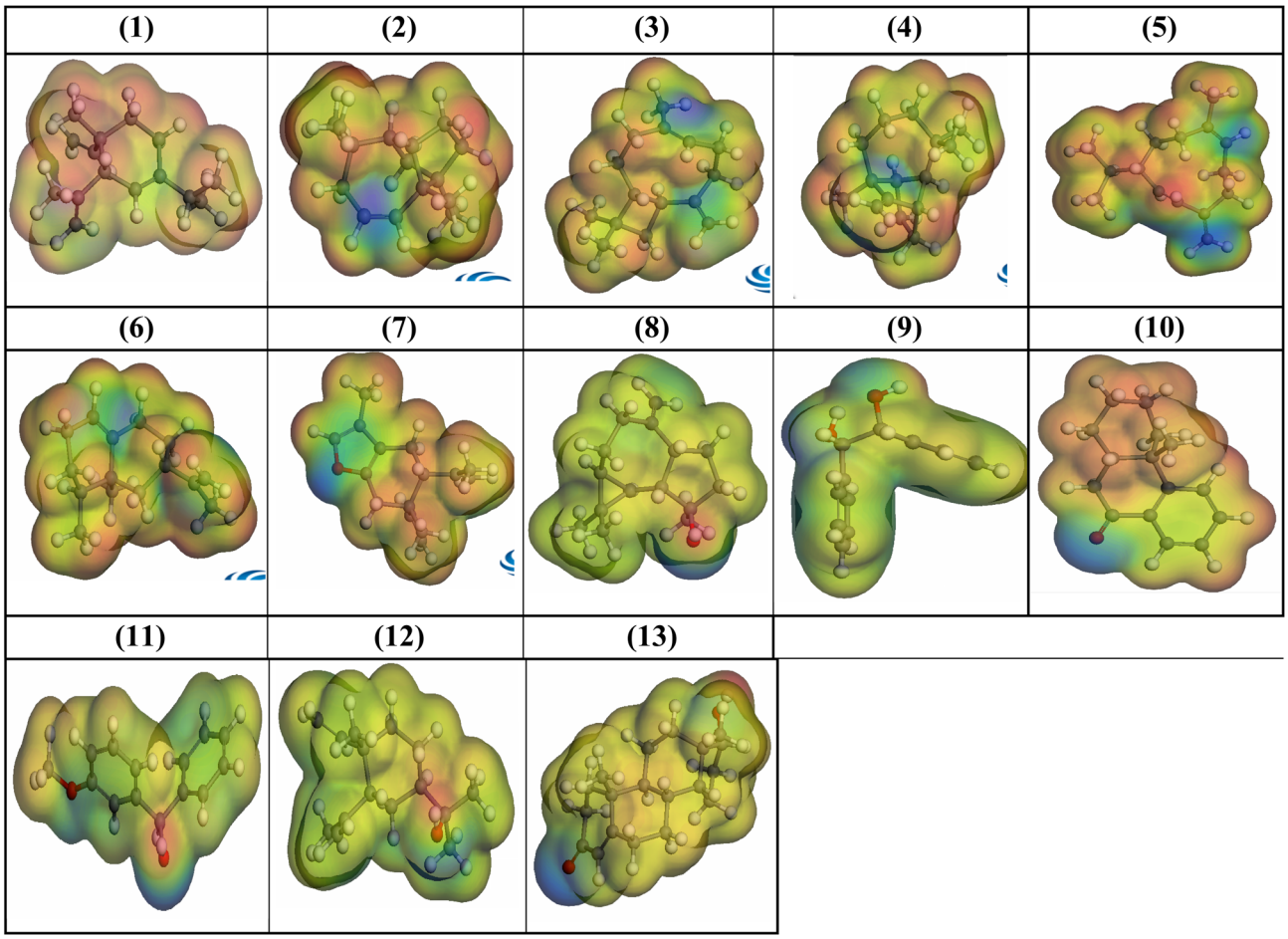

Fig. 22 Illustrations showing the nucleophilic attack on the H atoms (blue) of the 13 molecules of MRE.

chloride ions covering the SS surface and protonated MRE molecules (physisorption).[99] (ii) A protective layer is formed on the SS surface by the conjugated bonds of the aromatic rings and the unshared π-electrons of the inhibitor.[26] (iii) The presence of heteroatoms such as O that donate their lone pairs of electrons to the vacant d-orbital of Fe also forms a strong protective layer on its surface (chemisorption).[53]

Another interesting factor in this study that had a strong influence on the inhibition capacity was temperature. The results of this factor were surprising during the WL measurements shown in Table 2. The IE% value increased drastically from 77.6 to 93.6% with the temperature increasing from 25 to 55 °C, respectively, confirming the dominance of chemical adsorption at elevated temperatures. These results were also supported by the calculated ΔG_{ads} value of −41.78 kJ mol^{-1} at 55 °C (Table 3), indicating the formation of stable chemical bonds between the adsorbed MRE molecules and the SS surface.

An important issue that has not yet been discussed is the stability of MRE components in an acidic environment at high temperatures. Based on experimental results, there is no indication that the inhibitor molecules decompose under the reaction conditions here. The significant increase in the % IE value to 93.6% with increasing temperature to 55 °C, confirms the formation of stable chemical bond (chemisorption). In fact, the stability of an organic molecule is linked to its chemical bonds and structure. If organic molecules decompose, chemical bonds break, and new chemical species may form. XPS can identify the presence of these new species by detecting new peaks in the spectrum or changes in the relative peak intensities of the elements present, which was not the case with myrrh extract. Further support for the stability of MRE molecules under reaction conditions is that most of its components (Table 1), such as the phenanthrenone derivative (49.41%), include stable aromatic rings and functional groups (ketones, ethers).

Strictly speaking, this is a superior property of this inhibitor over others in industrial applications requiring high-temperature processes, such as: cleaning and polishing steel equipment, which is typically performed at temperatures between 50 and 60 °C, and oil well acidification, where the oil may be at the bottom of the well at high temperatures. In air coolers that operate at temperatures higher than ambient

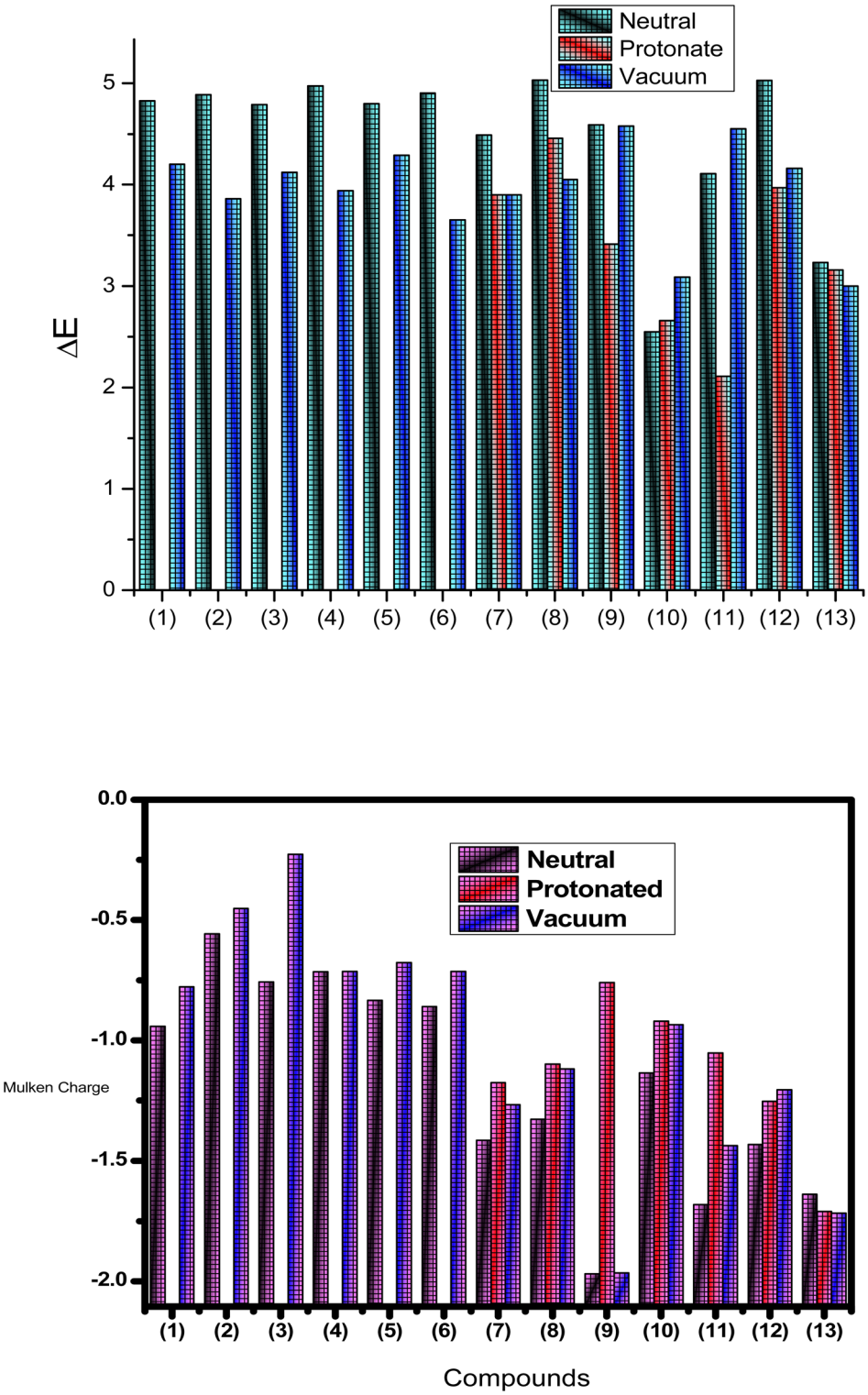

Fig. 23 Mulliken charges (MAC) and Δ*E* values for the 13 MRE molecules.

temperatures as well. Another advantage of this green inhibitor is its low cost compared to other inhibitors, as the percentage of myrrh plant extract reaches 15%, making it commercially and economically feasible and highly effective for the industrial sector. Strictly speaking, green inhibitors like MRE represent a more sustainable option because they are less harmful than their traditional counterparts.

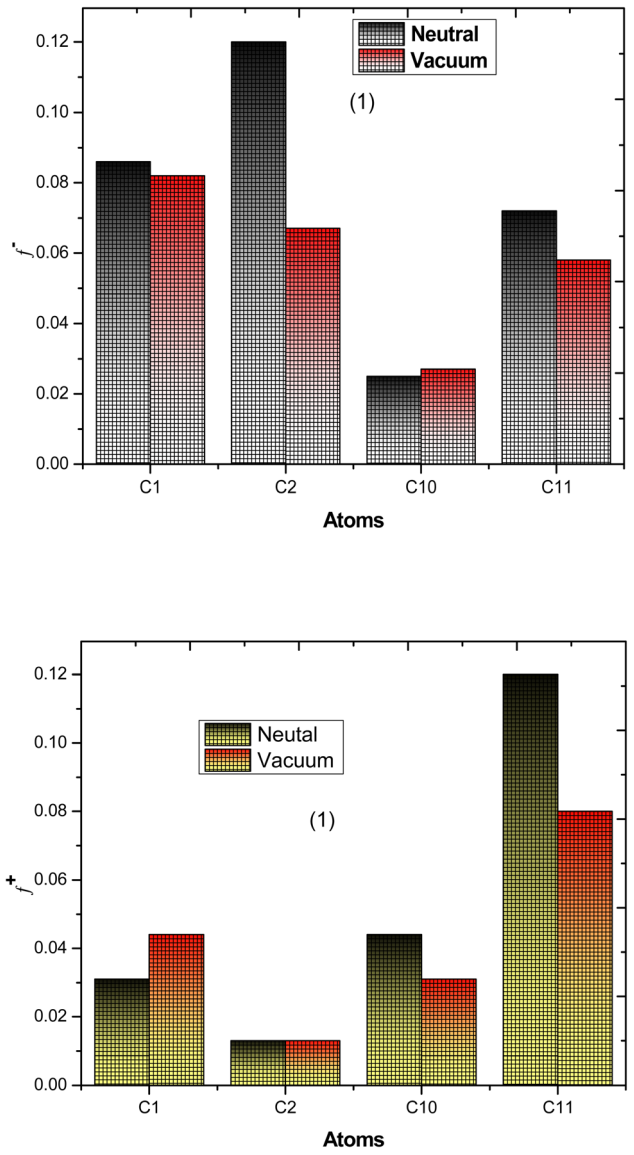

Fig. 24 Atomic structures of the MRE component (1), highlighting elevated values of Fukui functions (f_k^- and f_k^+).

4 Conclusions

Herein, green MRE extract was investigated as a potential corrosion inhibitor for SS in 1.0 M HCl solution at different temperatures using multifaceted experimental-computational methods. With the increase of MRE concentration and temperature, the inhibition efficiency increased dramatically. The Langmuir and Frumkin adsorption isotherms' models govern the myrrh extract's adsorption on the SS surface. The MRE functioned as a mixed-type inhibitor. As seen by XPS and AFM, a smooth and uniform protective layer from MRE particles was constructed on the SS surface. The thermodynamic and kinetic parameters were calculated and analyzed. The computational techniques provided more insights into the mechanism of inhibition of the myrrh extract. All experimental results of different techniques were in an excellent agreement with each other and with the employed computational methods. Green inhibitors, like MRE, represent a more sustainable option because they are less harmful than traditional inhibitors. The results of this study may have an impact on the rational development of a strong, effective, environmentally friendly, and inexpensive inhibitor for protecting metals in harsh acidic environments, fulfilling environmental, industrial, and economic aspirations.

Conflicts of interest

There are no conflicts to declare.

Data availability

The datasets generated and analyzed during this study are available from the corresponding author upon reasonable request.

Supplementary information is available. See DOI: **https://doi.org/10.1039/d5ra07138k**.

Acknowledgements

This work was supported and funded by the Deanship of Scientific Research at Imam Mohammad Ibn Saud Islamic University (IMSIU) (grant number IMSIU-DDRSP2502).

References

1 M. A. Quraishi, V. C. Srivastava, J. Pawan Kumar and M. A. Quraishi, PEG Cross-Linked Chitosan: A Biomacromolecule as Corrosion Inhibitor for Sugar Industry, *Int. J. Ind. Chem.*, 2018, **9**(4), 363–377, DOI: **10.1007/s40090-018-0165-0**.

2 A. Toghan, H. S. Gadow, A. Fawzy, H. Alhussain and H. Salah, Adsorption mechanism, kinetics, thermodynamics, and anticorrosion performance of a new thiophene derivative for C-steel in a 1.0 M HCl: Experimental and computational approaches, *Metals*, 2023, **13**, 1565.

3 A. Fawzy and A. Toghan, Inhibition evaluation of chromotrope dyes for the corrosion of mild steel in acidic environment: Thermodynamic and kinetic aspects, *ACS Omega*, 2021, **6**, 4051–4061.

4 A. Toghan, A. Fawzy, A. I. Alakhras and A. A. Farag, Electrochemical and theoretical examination of some imine compounds as corrosion inhibitors for carbon steel in oil wells formation water, *Int. J. Electrochem. Sci.*, 2022, **17**, 2212108.

5 H. S. Gadow, A. Fawzy, M. Khairy, M. M. S. Sanad and A. Toghan, Experimental and theoretical approaches to the inhibition of carbon steel corrosion by thiophene derivative in 1 M HCl, *Int. J. Electrochem. Sci.*, 2023, **18**, 100174.

6 A. Toghan, A. Fawzy, A. I. Alakhras, M. M. S. Sanad, M. Khairy and A. A. Farag, Correlating experimental with theoretical studies for a new ionic liquid for inhibiting corrosion of

carbon steel during oil well acidification, *Metals*, 2023, **13**, 862.

7 A. Toghan and A. Fawzy, Unraveling the adsorption mechanism and anti-corrosion functionality of dextrin and inulin as eco-friendly biopolymers for the corrosion of reinforced steel in 1.0 M HCl: A thermodynamic and kinetic approach, *Polymers*, 2023, **15**, 3144.

8 A. Fawzy, A. Toghan, N. Alqarni, M. Morad, M. E. A. Zaki, M. Sanad, A. I. Alakhras and A. A. Farag, Experimental and computational exploration of chitin, pectin and amylopectin polymers as efficient eco-friendly corrosion inhibitors for mild steel in acidic environment. Kinetic, thermodynamic and mechanistic aspects, *Polymers*, 2023, **15**(891), 2170576.

9 L. Popoola, A. Grema, G. Latinwo, B. Gutti and A. Balogun, Corrosion Problems during Oil and Gas Production and Its Mitigation, *Int. J. Ind. Chem.*, 2013, **4**(1), 35, DOI: **10.1186/2228-5547-4-35**.

10 M. Cui, X. Chen, S. Mei and S. Ren, Bioinspired Polydopamine Nanosheets for the Enhancement in Anti-Corrosion Performance of Water-Borne Epoxy Coatings, *Chem. Eng. J.*, 2023, **471**, 144760, DOI: **10.1016/j.cej.2023.144760**.

11 H. He, J. Shi, S. Yu, J. Yang, K. Xu, C. He and X. Li, Exploring Green and Efficient Zero-Dimensional Carbon-Based Inhibitors for Carbon Steel: From Performance to Mechanism, *Constr. Build. Mater.*, 2023, **411**, 134334, DOI: **10.1016/j.conbuildmat.2023.134334**.

12 F. Wang, J. Xu, Y. Xu, L. Jiang and G. Ma, A Comparative Investigation on Cathodic Protections of Three Sacrificial Anodes on Chloride-Contaminated Reinforced Concrete, *Constr. Build. Mater.*, 2020, **246**, 118476, DOI: **10.1016/j.conbuildmat.2020.118476**.

13 A. Khadom, A.; W. Hameed, K. Prevention of Steel Corrosion by Cathodic Protection Techniques, *Int. J. Adv. Chem. Technol.*, 2011, **4**(1), 17–30, DOI: **10.3923/ijct.2012.17.30**.

14 N. Sharma, S. Sharma, S. K. Sharma, R. L. Mahajan and R. Mehta, Evaluation of Corrosion Inhibition Capability of Graphene Modified Epoxy Coatings on Reinforcing Bars in Concrete, *Constr. Build. Mater.*, 2022, **322**, 126495, DOI: **10.1016/j.conbuildmat.2022.126495**.

15 A. Dehghani, G. Bahlakeh, B. Ramezanzadeh and M. Ramezanzadeh, Potential Role of a Novel Green Eco-Friendly Inhibitor in Corrosion Inhibition of Mild Steel in HCl Solution: Detailed Macro/Micro-Scale Experimental and Computational Explorations, *Constr. Build. Mater.*, 2020, **245**, 118464, DOI: **10.1016/j.conbuildmat.2020.118464**.

16 A. A. Farag, E. Mohamed and A. Toghan, The new trends in corrosion control using superhydrophobic surfaces: A review, *Corros. Rev.*, 2023, **41**, 21.

17 A. Fawzy, O. K. Alduaij, A. Al-Bahir, D. A. Alshammari, N. Alqarni, A. M. Eldesoky, A. A. Farag and A. Toghan, A comparative study of pyridine and pyrimidine derivatives based formamidine for copper corrosion inhibition in nitric acid: Experimental and computational exploration, *Int. J. Electrochem. Sci.*, 2024, **19**, 100403.

18 A. Fawzy, A. Toghan, O. K. Alduaij, N. Alqarni, A. M. Eldesoky and A. A. Farag, Electrochemical, spectroscopic, kinetic and surface analysis of the inhibitory performance of Alcian blue dye for copper corrosion in sulfuric acid solution, *Int. J. Electrochem. Sci.*, 2024, **19**, 100429.

19 A. Toghan, O. K. Alduaij, A. Fawzy, A. M. Eldesoky and A. A. Farag, Physicochemical, electrochemical, and theoretical study of the corrosion inhibition performance of copper using N-benzylhydrazinecarbothioamide in a 3.5% NaCl solution, *J. Electrochem. Sci. Eng.*, 2024, **14**, 231–245.

20 A. Fawzy, H. H. Alsharief, A. Toghan, A. Al Bahir, M. Alhasani, N. Alqarni, A. M. R. Alsaedi and T. A. Fargaly, Evaluation of protection performances of bis-oxindole-based derivatives for the corrosion of aluminum in acidic environment, *J. Mol. Struct.*, 2023, **1294**, 136443.

21 G. Bahlakeh, A. Dehghani, B. Ramezanzadeh and M. Ramezanzadeh, Highly Effective Mild Steel Corrosion Inhibition in 1 M HCl Solution by Novel Green Aqueous Mustard Seed Extract: Experimental, Electronic-Scale DFT and Atomic-Scale MC/MD Explorations, *J. Mol. Liq.*, 2019, **293**, 111559, DOI: **10.1016/j.molliq.2019.111559**.

22 A. Toghan, O. K. Alduaij, A. Fawzy, A. M. Mostafa, A. M. Eldesoky and A. A. Farag, Effect of adsorption and interactions of new triazole-thione-Schiff bases on the corrosion rate of carbon steel in 1 M HCl solution: Theoretical and experimental evaluation, *ACS Omega*, 2024, **9**, 6761–6772.

23 A. Toghan, O. K. Alduaij, A. Fawzy, A. M. Eldesoky and A. A. Farag, Physicochemical, electrochemical, and theoretical study of the corrosion inhibition performance of copper using N-benzylhydrazinecarbothioamide in a 3.5% NaCl solution, *J. Electrochem. Sci. Eng.*, 2024, **14**(2), 231–245.

24 A. Toghan, A. Fawzy, A. Al Bahir, N. Alqarni, M. M. S. Sanad, M. Khairy, A. I. Alakhras and A. A. Farag, Computational foretelling and experimental implementation of the performance of polyacrylic acid and polyacrylamide polymers as eco-friendly corrosion inhibitors for copper in nitric acid, *Polymers*, 2022, **14**, 4802.

25 A. Fawzy, A. Al Bahir, N. Alqarni, A. Toghan, M. Khider, I. M. Ibrahim, H. H. Abulreesh and K. Elbanna, Evaluation of synthesized biosurfactants as promising corrosion inhibitors and alternative antibacterial and antidermatophytes agents, *Sci. Rep.*, 2023, **13**, 2585.

26 H. M. Elabbasy, A. Toghan and H. S. Gadow, Cysteine as an Eco-Friendly Anticorrosion Inhibitor for Mild Steel in Various Acidic Solutions: Electrochemical, Adsorption, Surface Analysis, and Quantum Chemical Calculations, *ACS Omega*, 2024, **9**, 13391–13411.

27 A. Toghan, O. K Alduaij, N. Alqarni, E. M. Masoud, H. Alhussain, A. M. Mostafa, A. A. Farag and A. Fawzy, Mathematical, electrochemical, spectroscopic and microscopic monitoring of the adsorption effect of expired drugs on zinc corrosion in 3.5% NaCl solution, *Results Chem.*, 2025, **13**, 102006.

28 X. Q. Zeng, Z. N. Jiang, J. M. Duan, Y. R. Li, S. Y. Peng, C. F. Dong and G. A. Zhang, Developing a Novel Amino Acid Derivative as High-Efficient Green Corrosion Inhibitor for Mild Steel in Acidic Solution: Experiments and First-Principles Calculations, *Ind. Crops Prod.*, 2024, **210**, 118032, DOI: 10.1016/j.indcrop.2024.118032.

29 G. Bahlakeh, B. Ramezanzadeh, A. Dehghani and M. Ramezanzadeh, Novel Cost-Effective and High-Performance Green Inhibitor Based on Aqueous Peganum Harmala Seed Extract for Mild Steel Corrosion in HCl Solution: Detailed Experimental and Electronic/Atomic Level Computational Explorations, *J. Mol. Liq.*, 2019, **283**, 174–195, DOI: 10.1016/j.molliq.2019.03.086.

30 V. S. Sastri *Green Corrosion Inhibitors*; John Wiley & Sons, 2012.

31 A. Toghan, M. Gouda, K. Shalabi and H. M. Abd El-Lateef, Preparation, Characterization, and Evaluation of Macrocrystalline and Nanocrystalline Cellulose as Potential Corrosion Inhibitors for SS316 Alloy during Acid Pickling Process: Experimental and Computational Methods, *Polymers*, 2021, **13**, 2275.

32 N. Alqarni, B. El-Gammal, A. Fawzy, A. Al Bahir and A. Toghan, Investigation of expired ticarcillin and carbenicillin drugs for inhibition of aluminum corrosion in hydrochloric acid solution, *Int. J. Electrochem. Sci.*, 2022, **17**, 2212113.

33 M. Heikal, A. Ali, B. S. Ibrahim and A. Toghan, Electrochemical and Physico-mechanical Characterizations of Fly ash Composite Cements, *Constr. Build. Mater.*, 2020, **243**, 118309, DOI: 10.1016/j.conbuildmat.2020.118309.

34 A. Toghan, M. Khairy, M. Huang and A. A. Farag, Electrochemical, chemical and theoretical exploration of the corrosion inhibition of carbon steel with new imidazole-carboxamide derivatives in an acidic environment, *Int. J. Electrochem. Sci.*, 2023, **18**, 100072.

35 K. Bijapur, V. Molahalli, A. Shetty, A. Toghan, P. De Padova and G. Hegde, Recent trends and progress in corrosion inhibitors and electrochemical evaluation, *Appl. Sci.*, 2023, **13**, 10107, DOI: 10.3390/app131810107.

36 H. M. Abd El-Lateef, S. Shaaban, M. M. Khalaf, A. Toghan and K. Shalabi, Synthesis, experimental, and computational studies of water soluble anthranilic organoselenium compounds as safe corrosion inhibitors for J55 pipeline steel in acidic oilfield formation water, *Colloids Surf., A*, 2021, **625**, 126894.

37 A. Peter, I. B. Obot and S. K. Sharma, Use of Natural Gums as Green Corrosion Inhibitors: An Overview, *Int. J. Ind. Chem.*, 2015, **6**(3), 153–164, DOI: 10.1007/s40090-015-0040-1.

38 A. Zakeri, E. Bahmani and A. S. R. Aghdam, Plant Extracts as Sustainable and Green Corrosion Inhibitors for Protection of Ferrous Metals in Corrosive Media: A Mini Review, *Corros. Commun.*, 2022, **5**, 25–38, DOI: 10.1016/j.corcom.2022.03.002.

39 A. Rizi, A. Sedik, A. Acidi, K. O. Rachedi, H. Ferkous, M. Berredjem, A. Delimi, A. Abdennouri, M. ALAM, B. Ernst and Y. Benguerba, Sustainable and Green Corrosion Inhibition of Mild Steel: Insights from Electrochemical and Computational Approaches, *ACS Omega*, 2023, **8**(49), 47224–47238, DOI: 10.1021/acsomega.3c06548.

40 S. A. Gadir and I. M. Ahmed, Commiphora myrrha and commiphora Africana essential oils, *Int. J. Res. Pharm. Chem.*, 2014, **6**(7), 151–156.

41 L. O. Hanus, T. Rezanka, V. M. Dembitsky and A. Moussaieff, MYRRH–COMMIPHORA CHEMISTRY, *Biomed. Pap.*, 2005, **149**(1), 3–28.

42 S. Banerjee, V. Srivastava and M. M. Singh, Chemically modified natural polysaccharide as green corrosion inhibitor for mild steel in acidic medium, *Corros. Sci.*, 2012, **59**, 35–41, DOI: 10.1016/j.corsci.2012.02.009.

43 S. Abbout, D. Chebabe, M. Zouarhi, M. Rehioui, Z. Lakbaibi and N. Hajjaji, Ceratonia Siliqua L seeds extract as eco-friendly corrosion inhibitor for carbon steel in 1 M HCl: Characterization, electrochemical, surface analysis, and theoretical studies, *J. Mol. Struct.*, 2021, **1240**, 130611, DOI: 10.1016/j.molstruc.2021.130611.

44 H. S. Gadow, M. M. Motawea and H. M. Elabbasy, Investigation of MRE as a New Corrosion Inhibitor for α-Brass in 3.5% NaCl Solution Polluted by 16 Ppm Sulfide, *RSC Adv.*, 2017, **7**(47), 29883–29898, DOI: 10.1039/c7ra04271j.

45 K. F. Khaled, Application of Electrochemical Frequency Modulation for Monitoring Corrosion and Corrosion Inhibition of Iron by Some Indole Derivatives in Molar Hydrochloric Acid, *Mater. Chem. Phys.*, 2008, **112**(1), 290–300, DOI: 10.1016/j.matchemphys.2008.05.056.

46 K. F. Khaled, Evaluation of Electrochemical Frequency Modulation as a New Technique for Monitoring Corrosion and Corrosion Inhibition of Carbon Steel in Perchloric Acid Using Hydrazine Carbodithioic Acid Derivatives, *J. Appl. Electrochem.*, 2008, **39**(3), 429–438, DOI: 10.1007/s10800-008-9688-y.

47 A. S. Fouda, A. M. El-desoky and H. M. Hassan, Quinazoline Derivatives as Green Corrosion Inhibitors for Carbon Steel in Hydrochloric Acid Solutions, *Int. J. Electrochem. Sci.*, 2013, **8**(4), 5866–5885, DOI: 10.1016/s1452-3981(23)14728-6.

48 R. D. Alghamdi, L. S. Alqarni, M. D. Alghamdi, N. F. Alotaibi and H. Gadow, Experimental and Theoretical Investigations on the Use of Pumpkin Peel as a Sustainable Biomass Anticorrosion Agent for Aluminum in HCl Solutions, *J. Chem.*, 2024, **2024**, 1–26, DOI: 10.1155/2024/5696212.

49 A. Mustapha, O. Rachid, A. A. Youssef, A. O. Hicham, I. Rachid, N. Ayssar, A. Berisha, N. Z. Azzallou and M. Hamdani, Corrosion Inhibition of SS 316L by Organic Compounds: Experimental, Molecular Dynamics, and Conceptualization of Molecules–Surface Bonding in H2SO4 Solution, *Appl. Surf. Sci.*, 2023, **612**, 155755, DOI: 10.1016/j.apsusc.2022.155755.

50 M. Haneih, M. Azadi, N. Hassani, M. Neek-Amal, M. Rassouli and M. A. Bidi, The Inhibition Performance of Quinoa Seed on Corrosion Behavior of Carbon Steel in the HCl Solution; Theoretical and Experimental Evaluations, *J. Mol. Liq.*, 2021, **335**, 116183, DOI: 10.1016/j.molliq.2021.116183.

51 R. K. Mehta and M. Yadav, Corrosion Inhibition Properties of Expired Broclear Medicine and Its Carbon Dot as Eco-Friendly Inhibitors for Mild Steel in 15% HCl, *Mater. Sci. Eng. B*, 2023, **295**, 116566, DOI: 10.1016/j.mseb.2023.116566.

52 A. S. Fouda, M. A. Abd El-Ghaffar, M. H. Sherif, A. Taher El-Habab and A. El-Hossiany, Novel Anionic 4-Tert-Octyl Phenol Ethoxylate Phosphate Surfactant as Corrosion Inhibitor for C-Steel in Acidic Media, *Protect. Met. Phys. Chem. Surface*, 2020, **56**(1), 189–201, DOI: 10.1134/s2070205120010086.

53 A. Toghan, H. M. Dardeer, H. S. Gadow and H. M. Elabbasy, New promising halogenated cyclic imides derivatives as Potential Corrosion Inhibitors for Carbon Steel in Acidic Environment, *J. Mol. Liq.*, 2021, **325**, 115136–115156, DOI: 10.1016/j.molliq.2020.115136.

54 A. Toghan, A. Fawzy, N. Alqarni, A. Abdelkader and A. I. Alakhras, Inhibition effects of citrulline and glutamine for mild steel corrosion in sulfuric acid environment: Thermodynamic and kinetic aspects, *Int. J. Electrochem. Sci.*, 2021, **16**(1–21), 211118.

55 A. Toghan, A. Fawzy, A. I. Alakhras, N. Alqarni, M. E. A. Zaki, M. M. S. Sanad and A. A. Farag Experimental exploration, RSM modeling and DFT/MD simulations of the anticorrosion performance of naturally occurring amygdalin and raffinose for aluminum in NaOH solution, *Coatings*, 2023, **13**, 704.

56 W. Durnie, De M. Roland, A. Jefferson and B. Kinsella, Development of a Structure-Activity Relationship for Oil Field Corrosion Inhibitors, *J. Electrochem. Soc.*, 1999, **146**(5), 1751–1756, DOI: 10.1149/1.1391837.

57 M. El Faydy, R. Touir, M. Ebn Touhami, Z. Abdelkader, charafeddine Jama, L. Brahim, L. O. Olasunkanmi, E. E. Ebenso and B. Fouad, Corrosion Inhibition Performance of Newly Synthesized 5-Alkoxymethyl-8-Hydroxyquinoline Derivatives for Carbon Steel in 1 M HCl Solution: Experimental, DFT and Monte Carlo Simulation Studies, *Phys. Chem. Chem. Phys.*, 2018, **20**(30), 20167–20187, DOI: 10.1039/c8cp03226b.

58 N. D. Gowraraju, S. Jagadeesan, K. Ayyasamy, L. O. Olasunkanmi, E. E. Ebenso and C. Subramanian, Adsorption Characteristics of Iota-Carrageenan and Inulin Biopolymers as Potential Corrosion Inhibitors at Mild Steel/Sulphuric Acid Interface, *J. Mol. Liq.*, 2017, **232**, 9–19, DOI: 10.1016/j.molliq.2017.02.054.

59 A. S. Fouda, Effectiveness of Some Organic Compounds as Corrosion Inhibitors for Stainless Steel 201 in 1M HCl: Experimental and Theoretical Studies, *Int. J. Electrochem. Sci.*, 2018, **13**(10), 9826–9846, DOI: 10.20964/2018.10.36.

60 A. Toghan, A. A. Farag, O. K. Alduaij, H. M. Elabbasy, H. M. Dardeer, E. M. Masoud, A. Fawzy and H. S. Gadow, Electrochemical, gravimetric, quantum chemical and computational investigations on an effective synthetic chlorinated cyclic imide derivative as a corrosion inhibitor for carbon steel in sulfuric acid solution, *J. Mol. Struct.*, 2024, **1307**, 138040, DOI: 10.1016/j.molstruc.2024.138040.

61 A. Ostovari, S. M. Hoseinieh, M. Peikari, S. R. Shadizadeh and S. J. Hashemi, Corrosion Inhibition of Mild Steel in 1M HCl Solution by Henna Extract: A Comparative Study of the Inhibition by Henna and Its Constituents (Lawsone, Gallic Acid, α-d-Glucose and Tannic Acid), *Corros. Sci.*, 2009, **51**(9), 1935–1949, DOI: 10.1016/j.corsci.2009.05.024.

62 P. N. Devi, J. Sathiyabama and S. Rajendran, Study of Surface Morphology and Inhibition Efficiency of Mild Steel in Simulated Concrete Pore Solution by Lactic Acid–Zn2+ System, *Int. J. Corros. Scale Inhib.*, 2017, **6**(1), 18–31, DOI: 10.17675/2305-6894-2017-6-1-2.

63 A. Habibiyan, B. Ramezanzadeh, M. Mahdavian and M. Kasaeian, Facile size and chemistry-controlled synthesis of mussel-inspired bio-polymers based on Polydopamine Nanospheres: application as eco-friendly corrosion inhibitors for mild steel against aqueous acidic solution, *J. Mol. Liq.*, 2020, **298**, 111974, DOI: 10.1016/j.molliq.2019.111974.

64 H. M. Refat and A. A. Fadda, Synthesis and Antimicrobial Activity of Some Novel Hydrazide, Pyrazole, Triazine, Isoxazole, and Pyrimidine Derivatives, *J. Heterocycl. Chem.*, 2015, **53**(4), 1129–1137, DOI: 10.1002/jhet.2369.

65 A. S. Fouda, R. E. Ahmed and A. El-Hossiany, Chemical, Electrochemical and Quantum Chemical Studies for Famotidine Drug as a Safe Corrosion Inhibitor for α-Brass in HCl Solution, *Protect. Met. Phys. Chem. Surface*, 2021, **57**(2), 398–411, DOI: 10.1134/s207020512101010x.

66 H. M. A. El-Lateef, T. El-Dabea, M. M. Khalaf and A. M. Abu-Dief, Innovation of Imine Metal Chelates as Corrosion Inhibitors at Different Media: A Collective Study, *Int. J. Mol. Sci.*, 2022, **23**(16), 9360, DOI: 10.3390/ijms23169360.

67 H. M. Abd El-Lateef, A. H. Tantawy, K. A. Soliman, S. Eid and M. A. Abo-Riya, Novel Imine-Tethering Cationic Surfactants: Synthesis, Surface Activity, and Investigation of the Corrosion Mitigation Impact on Carbon Steel in Acidic Chloride Medium *via* Various Techniques, *Molecules*, 2023, **28**(11), 4540, DOI: 10.3390/molecules28114540.

68 Y. El Kacimi, M. A. Azaroual, R. Touir, M. Galai, K. Alaoui, M. Sfaira, M. Ebn Touhami and S. Kaya, Corrosion Inhibition Studies for Mild Steel in 5.0 M HCl by Substituted Phenyltetrazole, *Euro-Mediterr. J. Environ. Integr.*, 2017, **2**(1), DOI: 10.1007/s41207-016-0011-8.

69 S. Kr. Saha, M. Murmu, N. C. Murmu and P. Banerjee, Evaluating Electronic Structure of Quinazolinone and Pyrimidinone Molecules for Its Corrosion Inhibition Effectiveness on Target Specific Mild Steel in the Acidic Medium: A Combined DFT and MD Simulation Study, *J. Mol. Liq.*, 2016, **224**, 629–638, DOI: 10.1016/j.molliq.2016.09.110.

70 A. Singh, K. R. Ansari, D. S. Chauhan, M. A. Quraishi, H. Lgaz and I.-M. Chung, Comprehensive Investigation of Steel Corrosion Inhibition at Macro/Micro Level by Ecofriendly Green Corrosion Inhibitor in 15% HCl Medium, *J. Colloid Interface Sci.*, 2020, **560**, 225–236, DOI: 10.1016/j.jcis.2019.10.040.

71 K. R. Ansari and M. A. Quraishi, Experimental and Computational Studies of Naphthyridine Derivatives as Corrosion Inhibitor for N80 Steel in 15% Hydrochloric

Acid, *Phys. E*, 2015, **69**, 322–331, DOI: 10.1016/j.physe.2015.01.017.

72 B. K. Faris, A. A. Hassan, S. B. Aziz, M. A. Brza, A. M. Abdullah, A. A. Abdalrahman, O. A. Abu Ali and D. I. Saleh, Impedance, Electrical Equivalent Circuit (EEC) Modeling, Structural (FTIR and XRD), Dielectric, and Electric Modulus Study of MC-Based Ion-Conducting Solid Polymer Electrolytes, *Materials*, 2021, **15**(1), 170, DOI: 10.3390/ma15010170.

73 J. P. Sabawa and A. S. Bandarenka, Applicability of Double Layer Capacitance Measurements to Monitor Local Temperature Changes at Polymer Electrolyte Membrane Fuel Cell Cathodes, *Results Chem.*, 2020, **2**, 100078, DOI: 10.1016/j.rechem.2020.100078.

74 P. Cisquini, S. V. Ramos, P. R. P. Viana, V. de F. C. Lins, A. R. Franco and E. A. Vieira, Effect of the Roughness Produced by Plasma Nitrocarburizing on Corrosion Resistance of AISI 304 Austenitic Stainless Steel, *J. Mater. Res. Technol.*, 2019, **8**(2), 1897–1906, DOI: 10.1016/j.jmrt.2019.01.006.

75 I. H. Ali, Experimental, DFT and MD Assessments of Bark Extract of Tamarix Aphylla as Corrosion Inhibitor for Carbon Steel Used in Desalination Plants, *Molecules*, 2021, **26**(12), 3679, DOI: 10.3390/molecules26123679.

76 I. B. Obot and I. B. Onyeachu, Electrochemical Frequency Modulation (EFM) Technique: Theory and Recent Practical Applications in Corrosion Research, *J. Mol. Liq.*, 2018, **249**, 83–96, DOI: 10.1016/j.molliq.2017.11.006.

77 H. Ouici, M. Tourabi, O. Benali, C. Selles, charafeddine Jama, A. Zarrouk and F. Bentiss, Adsorption and Corrosion Inhibition Properties of 5-Amino 1,3,4-Thiadiazole-2-Thiol on the Mild Steel in Hydrochloric Acid Medium: Thermodynamic, Surface and Electrochemical Studies, *J. Electroanal. Chem.*, 2017, **803**, 125–134, DOI: 10.1016/j.jelechem.2017.09.018.

78 Y. Liu, Y. Hu, H. Hao and X. Zheng, Electrochemical and Theoretical Studies of Corrosion Inhibition Effect of Durio Zibethinus Peel Extract on Copper in the Artificial Seawater, *Int. J. Electrochem. Sci.*, 2022, **17**(3), 220343, DOI: 10.20964/2022.03.27.

79 M. Bouanis, M. Tourabi, A. Nyassi, A. Zarrouk, C. Jama and F. Bentiss, Corrosion Inhibition Performance of 2,5-Bis(4-Dimethylaminophenyl)-1,3,4-Oxadiazole for Carbon Steel in HCl Solution: Gravimetric, Electrochemical and XPS Studies, *Appl. Surf. Sci.*, 2016, **389**, 952–966, DOI: 10.1016/j.apsusc.2016.07.115.

80 A. Berrissoul, A. Ouarhach, F. Benhiba, A. Romane, A. Guenbour, B. Dikici, F. Bentiss, A. Zarrouk and A. Dafali, Assessment of Corrosion Inhibition Performance of Origanum Compactum Extract for Mild Steel in 1 M HCl: Weight Loss, Electrochemical, SEM/EDX, XPS, DFT and Molecular Dynamic Simulation, *Ind. Crops Prod.*, 2022, **187**, 115310, DOI: 10.1016/j.indcrop.2022.115310.

81 W. Temesghen and P. Sherwood, Analytical Utility of Valence Band X-Ray Photoelectron Spectroscopy of Iron and Its Oxides, with Spectral Interpretation by Cluster and Band Structure Calculations, *Anal. Bioanal. Chem.*, 2002, **373**(7), 601–608, DOI: 10.1007/s00216-002-1362-3.

82 A. Nahlé, R. Salim, F. El Hajjaji, M. R. Aouad, M. Messali, E. Ech-chihbi, B. Hammouti and M. Taleb, Novel Triazole Derivatives as Ecological Corrosion Inhibitors for Mild Steel in 1.0 M HCl: Experimental & Theoretical Approach, *RSC Adv.*, 2021, **11**(7), 4147–4162, DOI: 10.1039/d0ra09679b.

83 P. Mourya, P. Singh, A. K. Tewari, R. B. Rastogi and M. M. Singh, Relationship between Structure and Inhibition Behaviour of Quinolinium Salts for Mild Steel Corrosion: Experimental and Theoretical Approach, *Corros. Sci.*, 2015, **95**, 71–87, DOI: 10.1016/j.corsci.2015.02.034.

84 S. R. Ahamad, A. R. Al-Ghadeer, R. Ali, W. Qamar and S. Aljarboa, Analysis of inorganic and organic constituents of myrrh resin by GC–MS and ICP-MS: An emphasis on medicinal assets, *Saudi Pharm. J.*, 2017, **25**, 788–794, DOI: 10.1016/j.jsps.2016.10.011.

85 S. Y. Al-nami, A. M. Alturki and A. M. Wahba, Eco-Friendly Methanolic Myrrh Extract Corrosion Inhibitor for Aluminum in 1 M HCl, *ACS Omega*, 2023, **8**, 30917–30928, DOI: 10.1021/acsomega.3c02009.

86 I. Ichchou, L. Larabi, H. Rouabhi, Y. Harek and A. Fellah, Electrochemical Evaluation and DFT Calculations of Aromatic Sulfonohydrazides as Corrosion Inhibitors for XC38 Carbon Steel in Acidic Media, *J. Mol. Struct.*, 2019, **1198**, 126898, DOI: 10.1016/j.molstruc.2019.126898.

87 I. B. Obot, D. D. Macdonald and Z. M. Gasem, Density Functional Theory (DFT) as a Powerful Tool for Designing New Organic Corrosion Inhibitors. Part 1: An Overview, *Corros. Sci.*, 2015, **99**, 1–30, DOI: 10.1016/j.corsci.2015.01.037.

88 B. El Ibrahimi, A. Jmiai, K. El Mouaden, R. Oukhrib, A. Soumoue, S. El Issami and L. Bazzi, Theoretical Evaluation of Some α-Amino Acids for Corrosion Inhibition of Copper in Acidic Medium: DFT Calculations, Monte Carlo Simulations and QSPR Studies, *J. King Saud Univ. Sci.*, 2020, **32**(1), 163–171, DOI: 10.1016/j.jksus.2018.04.004.

89 P. K. Paul and M. Yadav, Investigation on Corrosion Inhibition and Adsorption Mechanism of Triazine-Thiourea Derivatives at Mild Steel/HCl Solution Interface: Electrochemical, XPS, DFT and Monte Carlo Simulation Approach, *J. Electroanal. Chem.*, 2020, **877**, 114599, DOI: 10.1016/j.jelechem.2020.114599.

90 I. Ahamad, R. Prasad and M. A. Quraishi, Adsorption and Inhibitive Properties of Some New Mannich Bases of Isatin Derivatives on Corrosion of Mild Steel in Acidic Media, *Corros. Sci.*, 2010, **52**(4), 1472–1481, DOI: 10.1016/j.corsci.2010.01.015.

91 S. Abd El Wanees, M. M. Kamel, M. Ibrahim, S. M. Rashwan, Y. Atef and M. G. Abd Elsadek, Corrosion Inhibition and Synergistic Effect of Ionic Liquids and Iodide Ions on the Corrosion of C-Steel in Formation Water Associated with Crude Oil, *J. Umm Al-Qura Univ. Appl. Sci.*, 2024, **10**, 107–119, DOI: 10.1007/s43994-023-00084-z.

92 A. Yurt, B. Duran and H. Dal, An Experimental and Theoretical Investigation on Adsorption Properties of Some

Diphenolic Schiff Bases as Corrosion Inhibitors at Acidic Solution/Mild Steel Interface, *Arab. J. Chem.*, 2010, **7**(5), 732–740, DOI: **10.1016/j.arabjc.2010.12.010**.

93 Y. Qiang, S. Zhang and L. Wang, Understanding the Adsorption and Anticorrosive Mechanism of DNA Inhibitor for Copper in Sulfuric Acid, *Appl. Surf. Sci.*, 2019, **492**, 228–238, DOI: **10.1016/j.apsusc.2019.06.190**.

94 A. Dounia, A. M. Soukaina, R. Bertani, M. M. Alanazi, G. Ennabety and M. Taleb, Experimental and Theoretical Investigation of the Inhibitor Efficiency of Eucalyptus Globulus Leaf Essential Oil (EuEO) on Mild Steel Corrosion in a Molar Hydrochloric Acid Medium, *Molecules*, 2024, **29**(14), 3323, DOI: **10.3390/molecules29143323**.

95 P. Singh, V. Srivastava and M. A. Quraishi, Novel Quinoline Derivatives as Green Corrosion Inhibitors for Mild Steel in Acidic Medium: Electrochemical, SEM, AFM, and XPS Studies, *J. Mol. Liq.*, 2016, **216**, 164–173, DOI: **10.1016/j.molliq.2015.12.086**.

96 Y. Boughoues, M. Benamira, L. Messaadia, N. Bouider and S. Abdelaziz, Experimental and Theoretical Investigations of Four Amine Derivatives as Effective Corrosion Inhibitors for Mild Steel in HCl Medium, *RSC Adv.*, 2020, **10**(40), 24145–24158, DOI: **10.1039/d0ra03560b**.

97 M. A. Albalawi and H. S. Gadow, Experimental and theoretical investigations on the use of Corchorus olitorius stem extract as a safe corrosion inhibitor for carbon steel in hydrochloric acid, *Egypt. J. Chem.*, 2024, **67**(9), 531–574, DOI: **10.21608/ejchem.2024.249091.8882**.

98 F. Cui, Y. Ni, J. Jiang, L. Ni and Z. Wang, Experimental and Theoretical Studies of Five Imidazolium-Based Ionic Liquids as Corrosion Inhibitors for Mild Steel in H_2S and HCl Solutions, *Chem. Eng. Commun.*, 2020, **208**(11), 1580–1593, DOI: **10.1080/00986445.2020.1802257**.

99 A. A. Farag and A. Toghan, Unravelling the adsorption and anti-corrosion potency of newly synthesized thiazole Schiff bases on C-steel in 1 M HCl: Computational and experimental implementations, *Results Eng.*, 2025, **25**, 104504, DOI: **10.1016/j.rineng.2025.104504**.